Silicification, flow pathways, and deep-seated hypogene dissolution controlled by structural and stratigraphic variability in a carbonate-siliciclastic sequence (Brazil)

Pisani, Luca; Antonellini, Marco; Bezerra, Francisco H.R.; Carbone, Cristina; Auler, Augusto S.; Audra, Philippe; La Bruna, Vincenzo; Bertotti, Giovanni; Balsamo, Fabrizio; More Authors

DOI
10.1016/j.marpetgeo.2022.105611

Publication date
2022

Document Version
Final published version

Published in
Marine and Petroleum Geology

Marine and Petroleum Geology 139 (2022) 105611

Contents lists available at ScienceDirect

Marine and Petroleum Geology

journal homepage: www.elsevier.com/locate/marpetgeo

Silicification, flow pathways, and deep-seated hypogene dissolution controlled by structural and stratigraphic variability in a carbonate-siliciclastic sequence (Brazil)

Luca Pisani [a,*], Marco Antonellini [a], Francisco H.R. Bezerra [b], Cristina Carbone [c], Augusto S. Auler [d], Philippe Audra [e], Vincenzo La Bruna [b], Giovanni Bertotti [f], Fabrizio Balsamo [g], Cayo C.C. Pontes [b], Jo De Waele [a]

[a] Bologna University, Department of Biological, Geological and Environmental Sciences, Via Zamboni 67, 40126, Bologna, Italy
[b] Programa de Pós-Graduação em Geodinâmica e Geofísica, Federal University of Rio Grande Do Norte, Natal, Brazil
[c] DISTAV, Dipartimento di Scienze della Terra, dell'Ambiente e della Vita, Università di Genova, Corso Europa 26, Genova, Italy
[d] Instituto Do Carste, Carste Ciência e Meio Ambiente, Belo Horizonte, Brazil
[e] Polytech'Lab UPR 7498, University Cote d'Azur, Nice, France
[f] Department of Geoscience and Engineering, Technical University of Delft, Netherlands
[g] Department of Chemistry, Life Sciences and Environmental Sustainability, University of Parma, Italy

ARTICLE INFO

Keywords:
Deep hydrothermal karst
Hypogene caves
Fluid flow
Karst reservoirs
Speleogenesis

ABSTRACT

Fractured and karstified carbonate units are key exploration targets for the hydrocarbon industry as they represent important reservoirs. Furthermore, large water reserves and geothermal systems are hosted in carbonate aquifers. This paper documents the relationships between stratigraphy, structural patterns, silicification, and the spatial-morphological organization of a 3D multistorey cave system developed in a Neoproterozoic mixed carbonate-siliciclastic sequence. We found that the combination of lithology, silicification, fracture patterns (controlled by lithostratigraphic variability), and petrophysical properties control the formation of high or low permeability zones; their distribution was fundamental for the spatial organization of dissolution and the compartmentalization of the resulting conduit system in different speleogenetic storeys. We propose a deep-seated hydrothermal origin for the fluids involved in the main phases of karst formation. Warm and alkaline hydrothermal fluids caused silica dissolution, followed by chalcedony and quartz reprecipitation in pore space and fractures. Rising fluids concentrated along through-going vertical fracture zones in the lower storey, whereas sub-horizontal bedding-parallel fluid flow was focused on sedimentary packages containing highly silicified dolostones (SiO_2>80 wt%) characterized by high permeability. The Calixto Cave is an enlightening example for the complex speleogenetic history affecting a mixed carbonate-siliciclastic succession where the combined effect of silicification and hydrothermal karst dissolution can potentially generate high-quality reservoirs.

1. Introduction

Silicification and karst dissolution in carbonate reservoirs are crucial processes that modify textures, mineralogy, and petrophysical properties of the host rock (Hesse, 1989; Lima et al., 2020; Souza et al., 2021). Karst features may be the result of rising fluid flow (hypogene speleogenesis; *sensu* Klimchouk, 2007), whose recharge and solutional efficiency are not connected to meteoric water percolation (i.e., epigene or supergene speleogenesis). The aggressivity of this rising flow is usually acquired from deep-seated sources, possibly associated with thermal processes, and is independent of soil or meteoric acids (Palmer, 2000; Audra and Palmer, 2015).

Many productive oil and gas deposits hosted in carbonate reservoirs are characterized by silicification and/or processes that can be assigned to hypogene karstification, like the Parkland field in Western Canada (Packard et al., 2001), the Tarim basin in China (Wu et al., 2007; Zhou

* Corresponding author.
E-mail addresses: lucapiso94@gmail.com (L. Pisani), marco.antonellini@unibo.it (M. Antonellini), hilario.bezerra@ufrn.br (F.H.R. Bezerra), carbone@dipteris.unige.it (C. Carbone), aauler@gmail.com (A.S. Auler), Philippe.AUDRA@univ-cotedazur.fr (P. Audra), vincenzolabruna@gmail.com (V. La Bruna), G.Bertotti@tudelft.nl (G. Bertotti), fabrizio.balsamo@unipr.it (F. Balsamo), cayopontes@gmail.com (C.C.C. Pontes), jo.dewaele@unibo.it (J. De Waele).

https://doi.org/10.1016/j.marpetgeo.2022.105611
Received 22 February 2022; Accepted 24 February 2022
Available online 1 March 2022

et al., 2014; Dong et al., 2018; You et al., 2018), pre-salt reservoirs in Santos and Kwanza basins (Girard and San Miguel, 2017; Poros et al., 2017), and Campos Basin offshore Brazil (De Luca et al., 2017; Lima et al., 2020). Networks of deep-seated conduits formed by dissolution are often intercepted during drilling in hydrocarbon exploration within soluble rocks (Maximov et al., 1984; Mazzullo et al., 1996; Mazzullo, 2004). The result is loss of fluid circulation or borehole collapse (Xu et al., 2017). Furthermore, carbonate aquifers constitute the most significant geothermal water resources worldwide (Goldscheider et al., 2010; Montanari et al., 2017) and important groundwater reserves (Ford and Williams, 2007).

Even if less common than conventional carbonate-hosted karst, hypogene speleogenesis has also been documented in silicified carbonates, quartz sandstones, and quartzite rocks (La Bruna et al., 2021; Sauro et al., 2014; Souza et al., 2021). Cavities enlarged by solution in quartzites were also described associated with hydrothermal Sb–Hg mineralization in Kirghizstan (Leven, 1961; Kornilov, 1978) and in Ukraine (Tsykin, 1989).

The presence of solutional voids and karst porosity in quartzites or highly silicified carbonates is thought to be common at depth where the solubility of silica is larger due to the high temperatures and alkalinity of circulating solutions (Lovering et al., 1978; Andreychouk et al., 2009; Sauro et al., 2014; Wray and Sauro, 2017; Klimchouk, 2019). However, in the existing literature, only few publications addressed the link between silicification and the stratigraphic-structural control on karst development, with its relative implications in the study of carbonate reservoirs (La Bruna et al., 2021; Souza et al., 2021). These studies focused on the main geological, diagenetic, and structural framework of the cave-hosting rocks, without exploring the speleogenetic mechanisms involved in the formation of solutional porosity.

In the past decades there has been a growing interest on the source of karst forming fluids, subsurface flow pathways, and geometry of the conduits' networks, with particular attention to deep hypogene speleogenesis (Klimchouk, 2007, 2009, 2019; Audra et al., 2009; De Waele et al., 2009, 2016; Audra and Palmer, 2015; Ennes-Silva et al., 2016; Klimchouk et al., 2016; Columbu et al., 2021; Spötl et al., 2021). Hypogene dissolution at depth has strong implications for carbonate reservoir properties and quality, given that the geometry of the conduits and their spatial distribution may focus fluid flow and generate strong heterogeneities in porosity and permeability (Klimchouk et al., 2016; Balsamo et al., 2020). The characterization of karst reservoir porosity is, therefore, a challenging task, also because most of the dissolution voids are below seismic resolution (Cazarin et al., 2019; Lyu et al., 2020; La Bruna et al., 2021). To fill this knowledge gap and optimize decision-making strategies in the conceptualization and characterization of karst reservoirs, detailed investigations on analog accessible caves are needed (Balsamo et al., 2020; Bertotti et al., 2020; La Bruna et al., 2021; Pisani et al., 2021; Pontes et al., 2021).

Karst porosity and permeability development can result from different processes. Several factors, such as lithology, hydrogeologic setting and source of aggressive fluids (epigene vs. hypogene), geological structures, stratigraphy, geochemistry, and climate contribute to the large variety of karst features, their morphologies, and the spatial organization of conduit networks (Klimchouk et al., 2000; Palmer, 2000; Ford and Williams, 2007). In carbonate sequences, fracture properties, pattern, and mechanical stratigraphy may affect hypogene karst development, given that fluid flow in low primary porosity rocks is mainly controlled by open discontinuities (i.e., joints) (Antonellini et al., 2014; Guha Roy and Singh, 2016; Lei et al., 2017; Lavrov, 2017; Giuffrida et al., 2019, 2020). The spatial arrangement of bedding interfaces, stratabound fractures, stylolites, fault zones, and through-going vertical fracture-zones generates a complex tridimensional network that controls fluid flow in hypogene conditions. In this context, mechanical stratigraphy and fracture distribution cause a strong anisotropy in the tridimensional organization of flow pathways, speleogenesis, and conduit geometry (Klimchouk et al., 2009, 2016; Klimchouk, 2019; Balsamo et al., 2020; La Bruna et al., 2021).

The objective of this work is to unravel the structural and stratigraphic controls on hypogene dissolution in a complex 3D cave network (Calixto Cave, Northeastern Brazil) characterized by silicification of carbonate layers. Following a multidisciplinary approach, quantitative structural analyses, stratigraphic, petrographic and petrophysical investigations on rock samples were used to characterize the sedimentary sequence in the cave. Furthermore, compositional analysis (XRD, XRF) and SEM-EDS investigations on cave mineral deposits and bedrock were performed to study silicification and solutional micro-textures. Combining this approach with a comprehensive geomorphological analysis of the conduit system, we assessed the role of structural-stratigraphic variability in controlling the karst-forming flow pathways and the resulting spatial-morphological organization of the conduit system. The results from this study may be of great interest for improving conceptual models of deep-seated hypogene dissolution in silicified carbonate units, allowing more reliable reservoir or aquifer reconstructions, and optimizing conceptual predictive models.

2. Study area

2.1. Geological setting

The Calixto Cave System (CCS) is a 1.4 km long and 55 m deep cave located in the Una-Utinga Basin in the São Francisco Craton (State of Bahia, Brazil) (Fig. 1).

The São Francisco Craton is the western portion of a large crustal block segmented during the Pangea breakup and the opening of the South Atlantic Ocean (Almeida et al., 2000; Misi et al., 2011). The Una-Utinga basin (Fig. 2A) hosts a sedimentary succession of Neoproterozoic age (Una Group), which overlies the Archean and Paleoproterozoic basement composed of metamorphic and igneous rocks (Fig. 2B). The Una-Utinga and the Irecê basins formed during rifting of the Rodinia supercontinent between 950 and 600 Ma (Condie, 2002). The Bebedouro *Fm*, composed of glacio-marine diamictites, marks the bottom of the Group (Misi and Veizer, 1998; Misi et al., 2011). The Salitre *Fm* overlies in stratigraphic unconformity the Bebedouro *Fm* and is characterized by a mostly carbonate succession with variable thickness (minimum 500 m), intercalated with siliciclastic or heterolithic beds (Misi, 1993; Misi et al., 2007, 2011; Santana et al., 2021).

Several geodynamic and tectonic events occurred in this area from ca. 740 to 560 Ma (Brito Neves et al., 2014). These events are broadly referred to as the Pan-African Cycle, or the *Brasiliano* Orogeny in South America (Teixeira et al., 2007). Strain in the Salitre *Fm* during the *Brasiliano* Orogeny resulted in a complex network of E-W- and NNE-SSW-trending deformed belts (Balsamo et al., 2020; Cazarin et al., 2021). These deformed belts include several fracture sets and a complex architecture of gentle folds characterized by fracture corridors localized in the hinge zone of the folds (Pontes et al., 2021). The most recent deformation events (540–510 Ma) were characterized by fissure magmatism and associated hydrothermal fluid flow along faults and fracture zones (Almeida et al., 2000; Guimarães et al., 2011; Klimchouk et al., 2016).

2.2. Hypogene caves and hydrothermal mineralization in the São Francisco Craton

The Una-Utinga and the Irecê basins host hundreds of karst systems, some of which are among the longest known in South America, with a combined cumulative length of over 140 km (Auler, 2017). Some of these karst systems developed in hypogene conditions by rising hydrothermal fluids that migrated upward through the fractured basement and that were horizontally confined by low-permeability (seal) layers (Klimchouk et al., 2016; Cazarin et al., 2019; Balsamo et al., 2020; Pontes et al., 2021). Following this, late-stage supergene sulfuric acid speleogenesis developed in shallow aquifers due to oxidation of bedrock

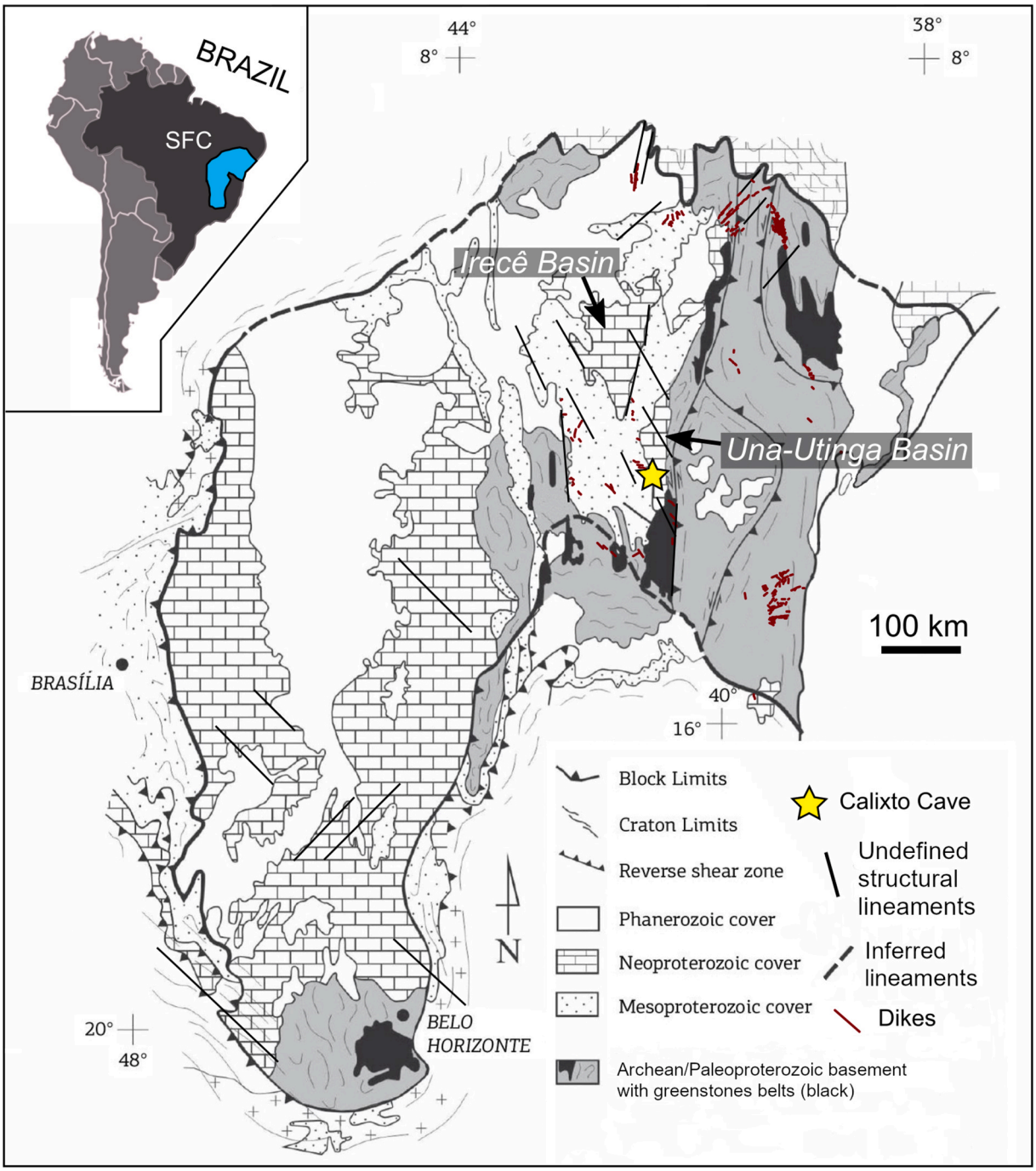

Fig. 1. Simplified geological map showing the location of the Calixto Cave system (CCS) and the main structural lineaments of the São Francisco Craton (light blue color in the inset; modified after Almeida et al., 2000; Peucat et al., 2011, and Misi et al., 2011). Dike lineaments in the Bahia region were extracted from the 1:1,000, 000 geological map of the State of Bahia (https://rigeo.cprm.gov.br/xmlui/handle/doc/8665). (For interpretation of the references to color in this figure legend, the reader is referred to the Web version of this article.)

sulfides (Auler and Smart, 2003).

Other works focused on silicified carbonate units and hypogene speleogenesis in the São Francisco Craton. Bertotti et al. (2020) highlighted the local development of caves associated with strike-slip fault zones and late silicification of dolostone layers (Morro Vermelho Cave, Irecê basin). North of the study area, in the Mesoproterozoic carbonates of Cabloco *Fm*, the Crystal Cave karst system shows dissolution features controlled by stratigraphy, deep tectonic structures, fracture corridors in fold hinges, and highly silicified layers (La Bruna et al., 2021; Souza et al., 2021). Furthermore, several cave systems in the Salitre *Fm* contain veins and deposits associated with hydrothermal mineral assemblages comprising quartz, chalcedony, barite, apatite, K-feldspar, hyalophane, iron oxides/hydroxides, iron-titanium oxides, and minor amounts of monticellite and diopside (Cazarin et al., 2019; Souza et al., 2021). Hydrothermal mineral assemblages and ore deposits have also been identified in the Una-Utinga and Irecê basins and their surrounding areas. These assemblages form Mississippi Valley-type (MVT) deposits containing quartz, sphalerite, barite, and galena (Kyle and Misi, 1997; Misi et al., 2012; Cazarin et al., 2021).

The Cambrian tectono-thermal event (~520 Ma) has been indicated as one of the probable drivers for hypogene speleogenesis in the Salitre *Fm* (Klimchouk et al., 2016). Late fracture reactivation and

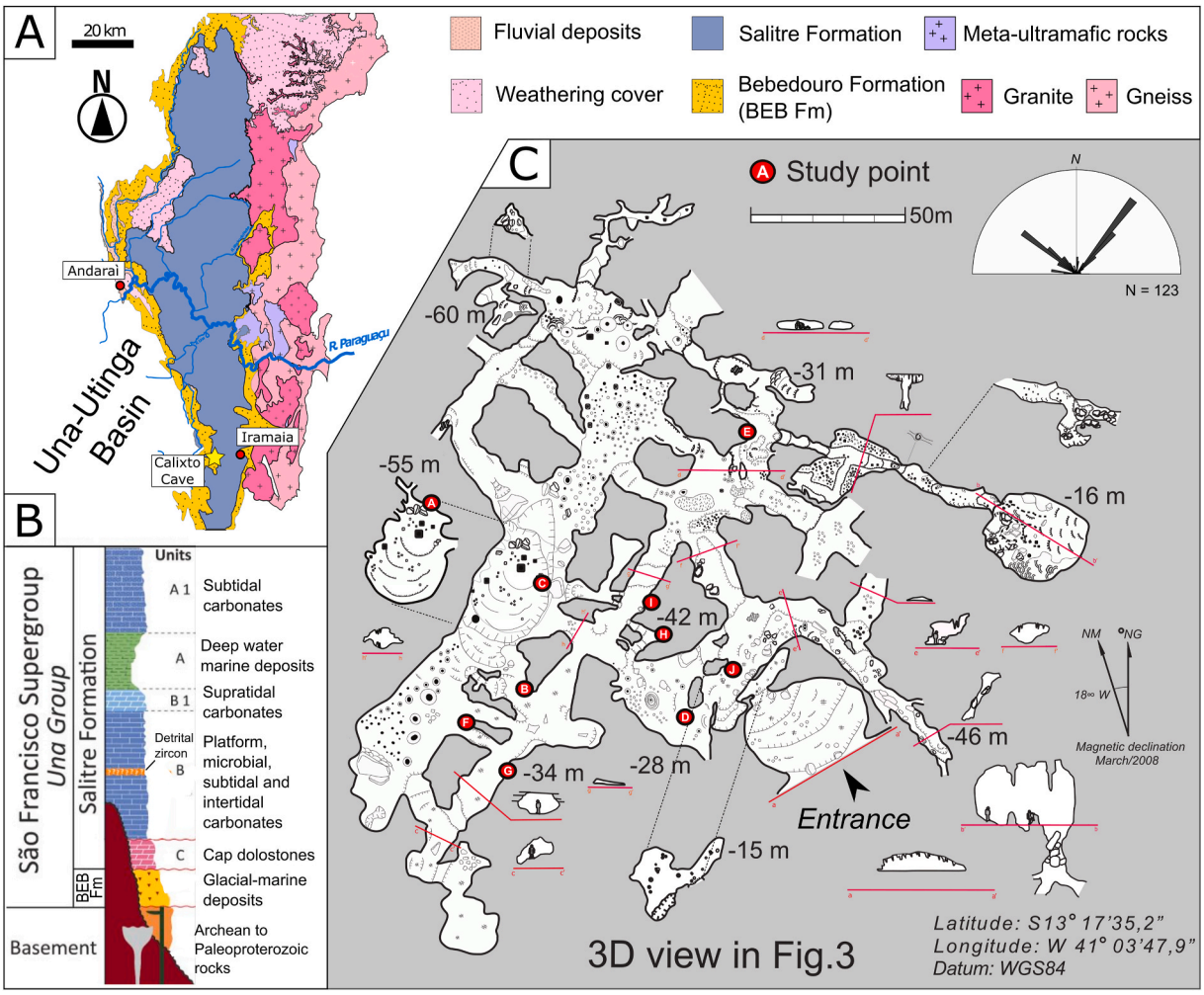

Fig. 2. A) Simplified geological map of the Una-Utinga basin. B) Simplified stratigraphic log of the main formations outcropping in the Una Group (modified from Santana et al., 2021). C) Topographic plan map of the CCS. The rose diagram in the right corner shows the frequency distribution of conduits' orientation. Red circles indicate study points and depth values are reported for different locations. Cave map acquired by *Grupo Pierre Marin de Espeleologia* (GPME) in 2008. The coordinates shown in the lower-right corner refer to the cave entrance. (For interpretation of the references to color in this figure legend, the reader is referred to the Web version of this article.)

hydrothermal events during the Pangea breakup in the Jurassic-Cretaceous have also been proposed for the cave systems located in the northern part of the craton (Klimchouk et al., 2016; Cazarin et al., 2019). Other studies (Bertotti et al., 2020; Souza et al., 2021) proposed that the interplay between Si-rich fluids and karstification happened in mesodiagenetic deep-seated conditions during the late Proterozoic. If this is true, the solutional cavities in the silicified carbonates of the São Francisco Craton would be among the oldest known on Earth.

3. Material and methods

3.1. Cave morphological and topographic analysis

Karst features are the result of mineral dissolution by fluid flow and fluid-rock interactions (Klimchouk et al., 2016). Morphologies and patterns of karst conduits, together with their infillings, are the fundamental attributes that reflect their origin and evolution. The spatial and morphological organization of the CCS conduits were analyzed by direct field investigation, detailed morphological observations, and the processing of a speleological topographic survey (Fig. 2C) made in 2008 by the *Grupo Pierre Martin de Espeleologia* (GPME).

The CCS morphology and geological features were studied and mapped in 10 representative sites (Fig. 2C) and systematically documented throughout the whole karst system. The morphological analysis of the CCS included the study of cave macro-morphology in plan, profile, and 3D view as well as the examination of spatial-temporal relationships between the identified morphological features and the local stratigraphy, structures, and former fluid flow pathways.

The cave survey was processed using the *cSurvey* software (https://www.csurvey.it/) to obtain a tridimensional, geographically referenced model corrected for the 2008 magnetic declination. The *cSurvey* software allows reconstructing the volumes of the cave by interpolation of azimuth, distance, and inclination measurements collected with a handheld modified Leica DISTOX laser-meter (Heeb, 2009). The *cSurvey* data were merged with the manually edited sketch maps drafted by the surveyor (Heeb, 2009; Lønøy et al., 2020; Pisani et al., 2021). With this approach, a raw 3D georeferenced model of the whole 1.4 km-long system was assembled. Following this step, the planimetry of the cave was processed in *ArcGis* software to manually measure the preferential direction of the conduits, normalized by the length of each cave segment (same method described in Pisani et al., 2019).

3.2. Stratigraphic and structural analyses

We performed a detailed lithological and sedimentary facies

description at several representative sites in the CCS (Fig. 2C) using outcrop observations and thin section petrographic analysis. Rock samples were collected using a geological hammer or a handheld electric driller to extract mini drill-cores from the cave walls (3.8 or 2.5 cm in diameter). 23 standard-thickness polished thin sections stained with blue epoxy were prepared and analyzed with an optical petrographic microscope both under transmitted and reflected light. Following the field and petrographic observations, the sedimentary sequence hosting the cave was subdivided in units, grouped according to their compositional and textural features. Carbonate rocks were classified based on their texture according to Dunham (1962) and Embry and Klovan (1971).

Structural measurements were collected in the survey points to unravel the nature, attitude, and kinematics of the observed fracture sets. Structural elements in the CCS were measured with classic geosurveying tools (compass and clinometer) and classified according to their type: open-mode fractures (joints and veins), pressure solution seams (stylolites), faults, and fracture zones (FZ; defined as zones of through-going clustered fractures with an intensity larger than the background of the host rock). Joints, veins, and FZ include stratabound (bedding confined) and non-stratabound (through-going) structures. Statistical analysis of fracture sets was performed with the *DAISY3* software plotting lower-hemisphere equal-area stereograms, rose diagrams, and frequency histograms (Salvini, 2004). Grouping of the different fracture sets was performed by calculating the best-fit Gaussian-curves for each cluster of orientations (Salvini, 2004; Del Sole et al., 2020).

Furthermore, fracture attributes were measured along 12 linear scanlines in 5 representative transects (Marrett et al., 1999; Ortega et al., 2006) to estimate fracture permeability from field data (Giuffrida et al., 2019, 2020). The following parameters were measured for each discontinuity along the transect: attitude, distance from the origin of the scanline, type, mechanic aperture, height (when measurable), roughness, and infilling (if present). Along the transects, we also calculated fracture linear intensity P_{10} (Ortega et al., 2006) and the coefficient of variation (Cv), defined as the ratio between the $\pm 1\sigma$ standard deviation and the mean value of fracture spacing of individual fracture sets (Odling et al., 1999; Zambrano et al., 2016; Pontes et al., 2021).

The mechanic aperture (B) and roughness coefficient (JRC) of the fractures were measured using analogical profile comparators developed by Barton and Choubey (1977), and Ortega et al. (2006). Estimates for permeabilities of individual fractures were obtained using the parallel-plate model approximation (Taylor et al., 1999; Philipp et al., 2013; Giuffrida et al., 2020). Hydraulic aperture (b) was computed by considering the JRC and by applying the following equation (1) (Barton and Choubey, 1977; Olsson and Barton, 2001; Giuffrida et al., 2020):

$$b = B^2 / JRC^{2.5} \quad (1)$$

Additionally, the real fracture spacing between individual features was calculated applying the Terzaghi method (1965).

The bulk permeability for each unit was then modeled as an Equivalent Porous Media (EPM; Taylor et al., 1999) combining the values of bedding-normal and bedding-parallel rock plugs permeability (considered equivalent to matrix permeability), fracture spacing, and estimated fracture permeability of individual sets. Bedding-parallel average permeability normal to the main fracture sets (K_N) and bedding-normal average permeability parallel to the main fracture sets (K_P) were calculated based on an elementary cubic volume of 1 m side using the equations described in Freeze and Cherry (1979) and reported in the Supplementary Material section of this article.

Given that natural fractures are neither smooth nor parallel, the reliability of applying the parallel-plate model to compute fracture permeability must be carefully considered (Zhang, 2019). Since our purpose was limited to evaluate the relative variability in fracture patterns and properties within the different sedimentary units, we did not perform any further analysis. Stochastic fracture aperture distribution and numerical modelling to upscale or calculate equivalent fracture permeability at confining pressure (Cacas et al., 1990; Flodin et al., 2004; Antonellini et al., 2014; Bisdom et al., 2016; Zheng et al., 2020; Smeraglia et al., 2021) are beyond the scope of this work.

3.3. X-ray analyses

Eighteen rock samples from the sedimentary sequence exposed in the cave were collected and analyzed to measure the major (>1 g/100 g) and minor (0.1–1.0 g/100 g) compounds with X-ray fluorescence (XRF). The powdered samples were analyzed with a sequential wavelength dispersive XRF spectrometer equipped on a Malvern Panalytical - model Zetium. The analyses were performed after STD-1 calibration and the values were normalized to 100 wt%. Finally, loss of ignition (LOI) was calculated heating the samples at 1020 °C for 2 h. The main mineral phases were also investigated with an Empyrean-Panalytical X-ray diffractometer mounting a Cu-anode (λ=1.542 Å; 2.2 kW, range 2θ=2.5–70°, step size =0.02° 2θ) at the *Laboratório de Caracterização Tecnológica* from the University of *São Paulo* (Brazil). The identification of crystalline phases was performed using the standard dataset of the PDF2 database from the ICDD (International Centre for Diffraction Data) and ICSD (Inorganic Crystal Structure Database). XRD analyses were also performed on selected samples of cave sediments at the *Laboratório do Centro de Tecnologias do Gás e Energias Renováveis-LTG-ER, Laboratório de Ensaios de Materiais* (Lagoa Nova, Brazil) with a Shimadzu XRD-6000 X-ray diffractometer mounting a Cu-anode (current: 20 mA, voltage =40 kV, range 2θ=5–80°, step size =0.02° 2θ).

3.4. SEM-EDS analyses

SEM-EDS analyses were carried out on five selected polished thin-sections from highly silicified rocks with a Tescan Vega 3 LMU equipped with an Energy Dispersive Spectroscopy (EDS) EDAX Apollo-X SDD detector, at 20 kV accelerating voltage, 1.2 nA beam current, and 5–10 μm beam diameter, operating at the DISTAV Department of the University of Genova. Additionally, *in situ* SEM analyses on eight silicified bulk rock fragments were performed at the BIGEA Department of the University of Bologna with a JEOL JSM-5400 equipped with an IXRF system for X-ray EDS spectroscopy to evaluate the microtexture and morphologies of quartz grains. All samples were prepared with gold coating and imaged both as backscattered electron (BSE) images or secondary electron (SE) images.

3.5. Petrophysical properties

Petrophysical analyses were performed to measure porosity, permeability, density, and pore volume on 50 rock plugs covering the whole stratigraphic sequence exposed in the cave. The analyses were performed using a *Coreval 700* unsteady-state gas permeameter and porosimeter at the *LABRES-Departamento de Engenharia de Petróleo* of the *Universidad Federal do Rio Grande do Norte*. Petrophysical properties were measured on 2.5 cm-diameter and 3 cm-high rock plugs cut from mini-drill cores extracted from the cave walls. For each unit, parallel and normal (or oblique) to bedding samples were collected to quantify the permeability tensor. The pore volume calculations were made in a N_2 gas injection porosimeter at a confining pressure of 600 psi. Additionally, the Klinkenberg correction was applied to calculate the permeability in mD (Klinkenberg, 1941; Araújo et al., 2021).

4. Results

The results of our multidisciplinary study in the CCS are reported in the following sections. The sedimentary and speleogenetic units in the cave are presented moving from bottom to top of the sequence, describing their main sedimentary, petrographic, compositional, and

geomorphological characteristics. Microtextural, and mineralogical data associated with the silicified units are illustrated. Finally, the structural and petrophysical properties of the different sedimentary and speleogenetic units are shown.

4.1. Sedimentary and speleogenetic units in the CCS

The sedimentary sequence exposed in the CCS includes the following sedimentary units (Fig. 3A): (A) dolostones with tabular cross-stratification, (B1) highly silicified dolostones, (B2) heteroliths, (B3) siliciclastic tempestites, and (C) cherty dolostones. The bulk chemical and mineralogical compositions of 18 samples from the entire sedimentary succession and of four cave sediment samples are reported in the Supplementary Material of this article. XRF results are also reported in the diagrams of Fig. 4.

Based on its topography and tridimensional organization (Fig. 3), the CCS can be classified as a 3D multistorey cave system (Audra et al., 2009; Audra and Palmer, 2015). The spatial organization of the conduit system and its morphology are strongly heterogeneous and reflect the vertical stratigraphic variations in the sedimentary column. Four speleogenetic units, grouped based on their morphological, geometric, and genetic characteristics, are defined from bottom to top as: lower storey (Fig. 3B), middle storey (Fig. 3C), upper storey (Fig. 3D), and doline entrance (Fig. 3E).

The network of conduits shows four clustered orientation trends in map view (Fig. 2C): the NE-SW (N35E-N45E) and NW-SE (N125E-N135E) trends are the most frequent whereas the N–S (N0E-N10E) and E-W (N90E-N100E) are secondary trends. The cave does not show the typical geomorphic features deriving from epigenic speleogenesis (i.e., lack of surface-derived sedimentation, vadose speleogens, scallops or

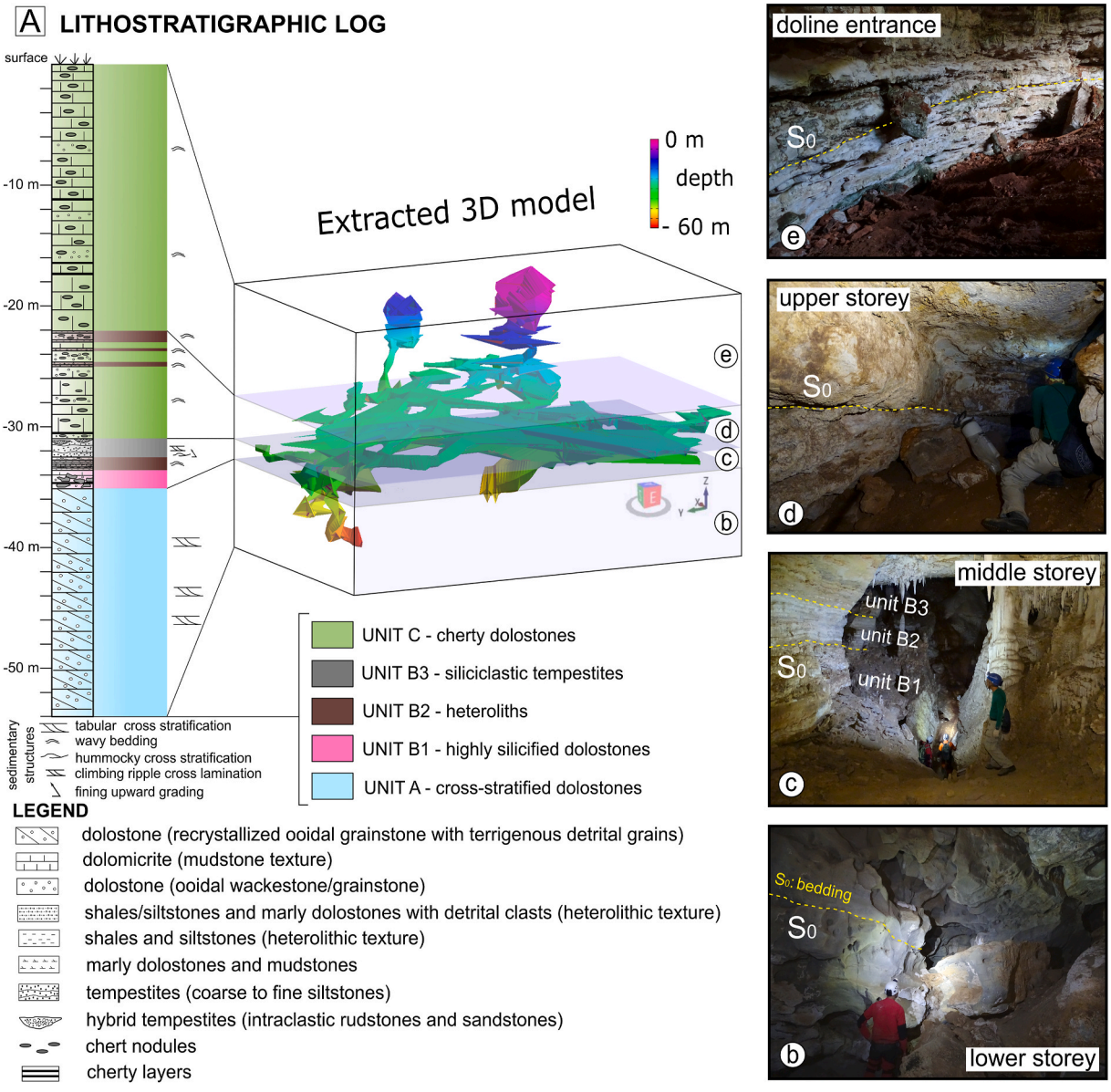

Fig. 3. A) Lithostratigraphic log of the sedimentary sequence exposed in the CCS, subdivided according to the units described in the main text. The 3D model extracted from the topographic survey of the cave is also shown. B) Lower storey typical morphologies, with phreatic spongework patterns, blind-ending passages, and rising conduits. White crusts covering the walls are calcite coralloids. C) Middle storey morphology with sub-elliptical or sub-rounded stratigraphically confined conduits. The longest and most developed sector of the CCS (expressed with green colors in the 3D model) belongs to this unit. D) Typical shapes and dimensions of the upper storey with small secondary passages. Condensation-corrosion features are commonly observed next to the entrance. E) Collapsed doline entrance. Red soil and debris are transported in the upper sector of the CCS by recent but ephemeral mudflows and streams. Bedding (S_0) is shown with dashed yellow lines. (For interpretation of the references to color in this figure legend, the reader is referred to the Web version of this article.)

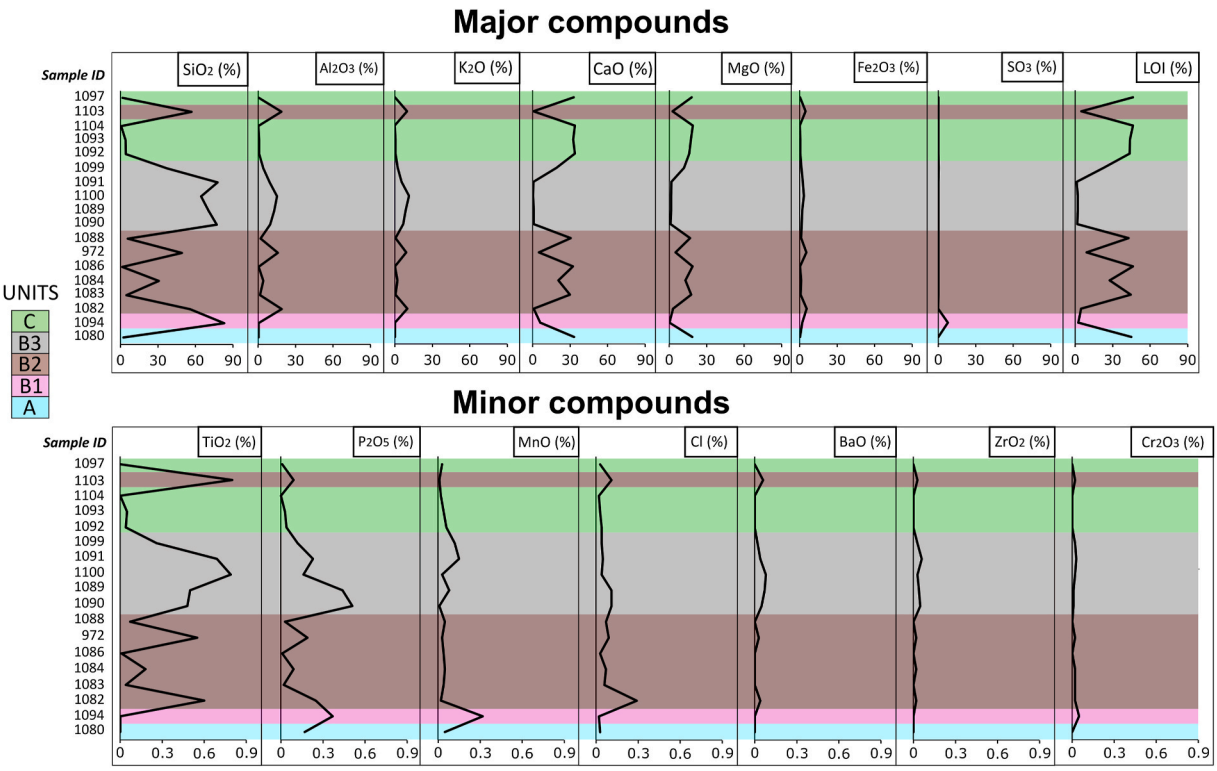

Fig. 4. XRF bulk rock chemical composition of 18 representative hand samples collected in the cave and grouped according to their sedimentary unit. For the detailed description of the samples, the reader is referred to the Supplementary Material of the article.

notches, etc.) and any link to surface geomorphology and drainage, except for the collapsed doline entrance. The typical cave sediments in the CCS are authigenic, deriving from block collapse or degradation by condensation-corrosion of the host rock. Secondary minerals resulting from guano-related processes (gypsum crystals and powders, phosphate crusts) are also present.

4.1.1. *Lower storey – unit A*

The lower storey spans from the cave bottom to 35 m depth relative to the surface. The rocks exposed are medium to thick beds of dolostones with tabular cross-stratification (Fig. 5A). Bedding-parallel stylolites are commonly observed, and they define the mechanical layering (spacing from a few cm up to 60–80 cm). This storey is characterized by vertical chambers with spongework morphologies (Fig. 3B), rising conduits, cupolas, blind ending passages, and rift-like discharge feeders localized along the intersection of multiple fracture sets, faults, or FZ (Fig. 5C). Such geomorphic features are typical (but not exclusive) of hypogene caves (Klimchouk, 2007, 2019; Audra et al., 2009; De Waele et al., 2009, 2016; Audra and Palmer, 2015). Fractures controlling the localization of feeders and rising conduits often present cm-wide reactive fronts (Fig. 5B) and bleaching halos (whitening fabric due to fluid-rock interactions indicating mobilization of metal ions; Ming et al., 2016).

Dolostones have a crystalline texture (Fig. 5D) deriving from the dolomitization of pristine ooidal grainstones (or less common wackestones) with terrigenous detrital clasts (mainly sub-rounded quartz grains, Fig. 5E) and fine pyrite crystals, often replaced by pseudomorphs of iron-oxides and hydroxides. The original ooidal texture is occasionally visible in thin sections (Fig. 5E). Porosity is mainly represented by vuggy, moldic or intercrystalline pores, often filled by euhedral mega-quartz, K-feldspar (microcline) or apatite crystals (Fig. 5D and F). White crusts of coralloid calcite growing on the dolostone rock characterize the cave walls at the bottom of the lower storey (Fig. 3B).

4.1.2. *Middle storey – units B1, B2 and B3*

The middle storey includes the most interesting and longest portion of the CCS, characterized by a maze network of sub-horizontal galleries developed between 35 and 31 m of depth from the surface. This section contains a mixed carbonate-siliciclastic interval (~4 m-thick, Fig. 6A) hosting ~80% of the entire cave passages.

The lower part of the middle storey is developed in unit B1, a 1.8 m-thick dolostone pack, with ooidal wackestone or mudstone (dolomicrite) textures, characterized by intense silicification (SiO_2>80 wt%, Fig. 4). Layering and ooidal structures are rarely preserved. Micro-crystalline quartz (defined as Qtz-A, forming chert) is concentrated in nodules or irregular layers replacing the dolomite grains (Fig. 6B and C) and as cement between residual dolomite often associated with iron oxides and less frequently with pyrite. Residual dolostone and Qtz-A (chert) show abundant vuggy and fracture porosity. Open fractures and vuggy pores are partially filled with euhedral blocky mega-quartz (Qtz-B) and chalcedony quartz (Qtz-C), both having mineral inclusions that will be further described in the following sections.

The highly silicified package is sealed by unit B2, a 0.9 m-thick interval characterized by the alternation of thin heterolith layers (defined as a sedimentary structure made up of interbedded deposits of sand/silt and mud formed in a tidal environment; Reineck and Wunderlich, 1968), marly dolostones with detrital clasts, and dolomicrites with chert nodules (Fig. 6D and E). Heteroliths are composed of mm-thick intercalations of mud and silt with wavy bedding (Fig. 6D) or dolostones with ooidal grainstone texture with terrigenous detrital clasts and coarse silt grain size. Pyrite crystals and their iron oxides/hydroxides associated pseudomorphs are common in unit B2.

This heterolithic facies is capped by a 1.1 m-thick interval (unit B3) of graded coarse-to-fine siltstones (Fig. 6F) organized in a rhythmic sequence with (from bottom to top) parallel lamination, hummocky-cross-stratification, and cross-lamination with climbing ripples, identified as a tempestite facies (Myrow and Southard, 1996). In the upper part of the unit, some hybrid carbonate-siliciclastic tempestites show

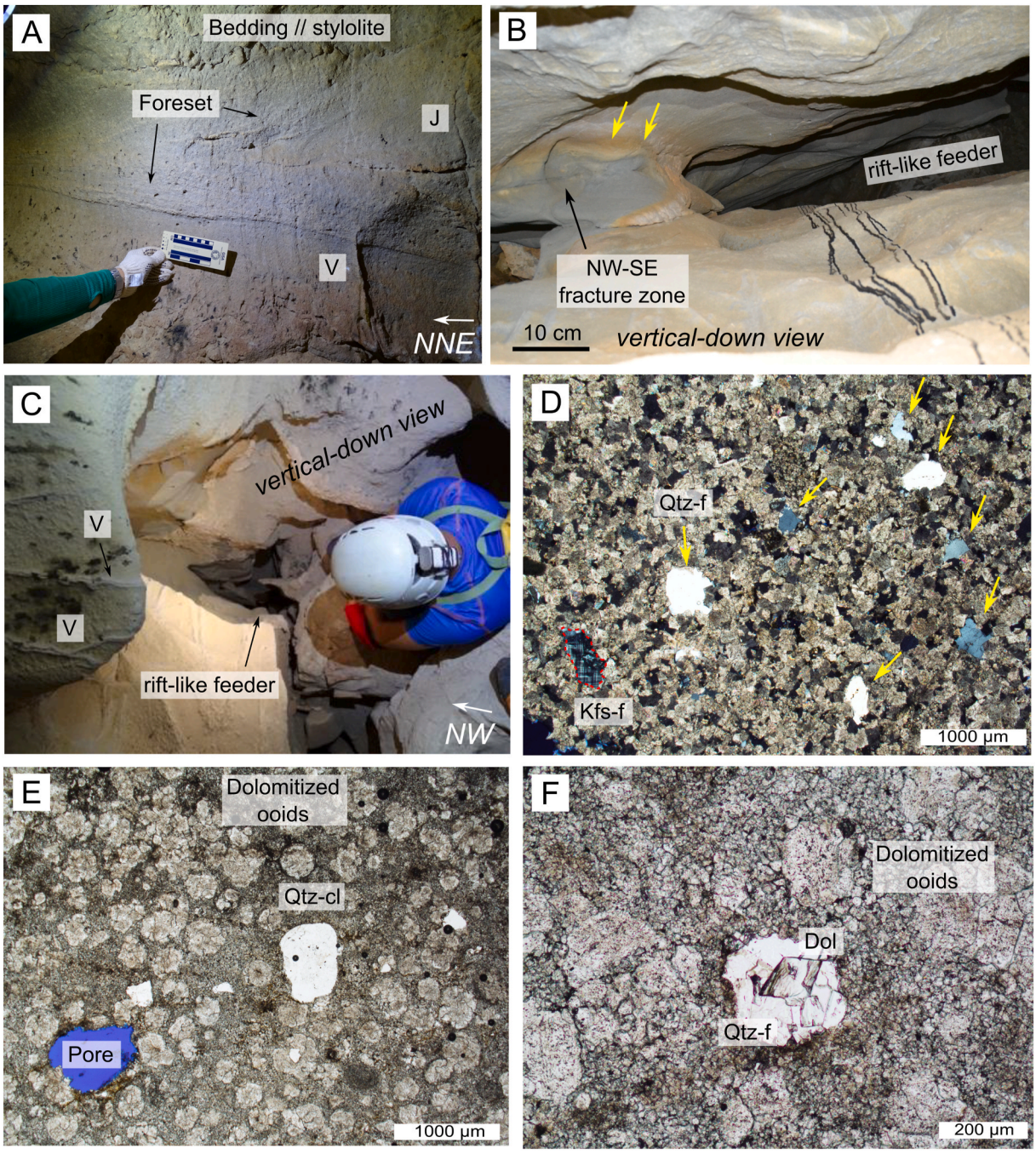

Fig. 5. Mesoscale (outcrop) and microscale (thin section) observations in the lower storey developed in unit A. A) Tabular cross-stratification with foresets occasionally preserved from the dolomitization process. B) Vertical-down view of a typical rift-like feeder localized on a NW-SE striking fracture zone composed of subparallel joints with bleaching reactive halos (pointed by the yellow arrows). C) Vertical-down view of a rift-like feeder localized at the intersection between NW-SE and N–S striking fracture zones. Nearby fractures are boxwork veins filled with quartz. D) Dolostone with crystalline texture and vuggy porosity filled with mega-quartz crystals (indicated by yellow arrows) and K-feldspar (microcline with typical cross-hatched twinning). Image under cross-polarized light. E) The original ooidal grainstone texture is occasionally preserved in the dolostone. Sub-rounded terrigenous detrital quartz is common in unit A. Image under parallel-polarized light. F) Detail of the dolomite grains and cement, with moldic porosity filled by quartz. Relict euhedral dolomite grains are included in the quartz cement. Image under parallel-polarized light. Label abbreviations: J (joint), V (veins), FZ (fracture zone), Qtz-f (mega-quartz fillings), Kfs-f (K-feldspar fillings), Qtz-cl (quartz detrital clast), Dol (dolomite). (For interpretation of the references to color in this figure legend, the reader is referred to the Web version of this article.)

massive, graded beds of intraclastic rudstones and coarse sandstones with carbonate intraclasts and dolomitized ooids (Fig. 6G). Iron oxide and hydroxide stains are commonly found in the tempestite facies (Fig. 6F).

The middle storey is a vast network of sub-horizontal passages with a maze pattern, connected to the lower storey by rising narrow feeders or conduits (Fig. 7A). The main horizontal galleries are confined in the highly silicified unit B1, below the heterolithic/siliciclastic interval of units B2 and B3 (Fig. 7B). Just below unit B2, there are extensive mega-quartz (Qtz-B) or chalcedony (Qtz-C) mineral deposits filling vuggy pores and veins (Fig. 7A). Most of these quartz-rich mineral deposits are associated with pore space developed in the micro-crystalline quartz facies (chert, Qtz-A) or, secondarily, in the residual dolostone facies (Fig. 7C).

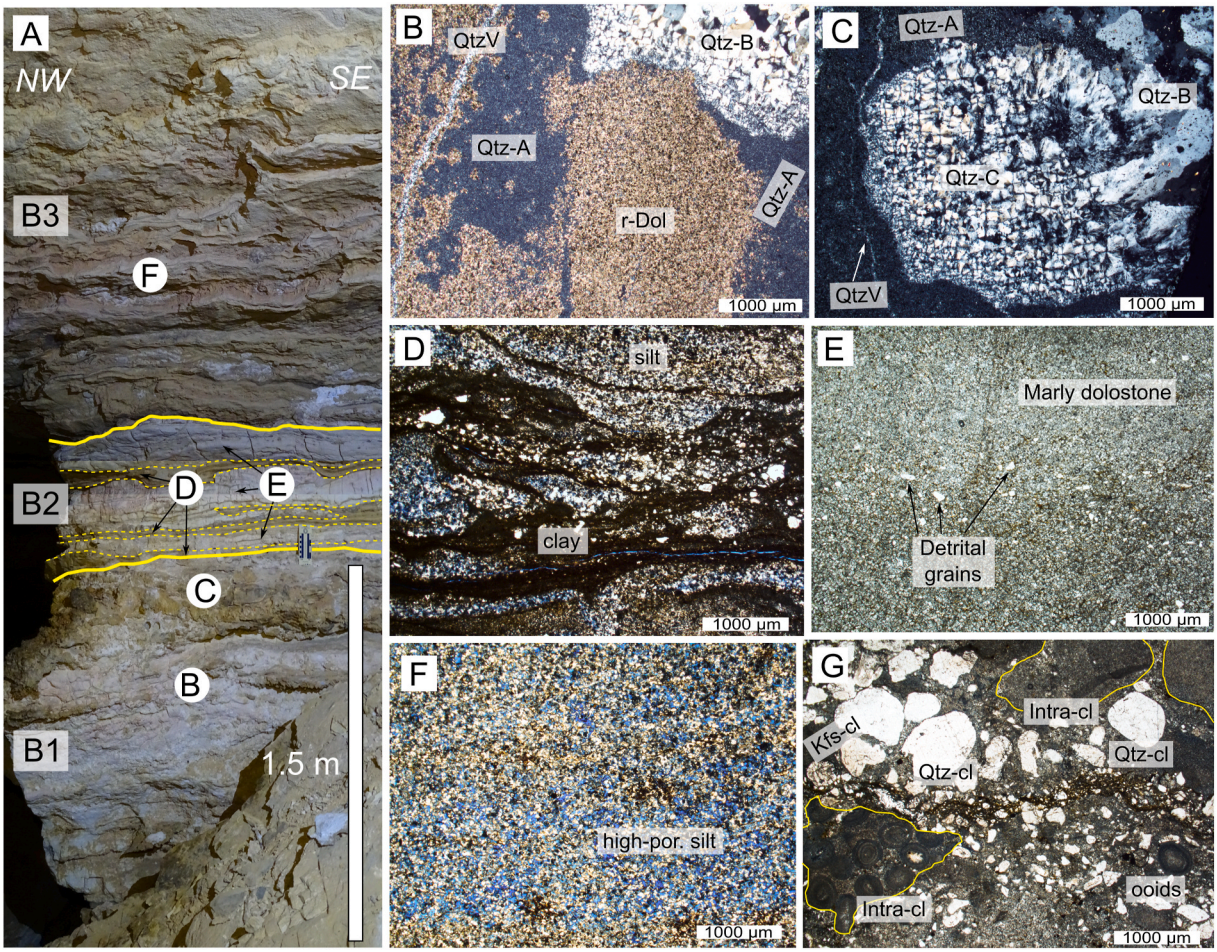

Fig. 6. Mesoscale (outcrop) and microscale (thin section microphotographs) observations in the middle storey developed in units B1, B2, and B3. A) Outcrop view of the sedimentary interval between unit B1 and unit B3. Letters in the circles point to the locations of the microphotographs displayed in this figure. B–C) Micro-crystalline quartz (Qtz-A) replacing dolomite grains and cement in unit B1. Solutional pores and enlarged fractures are filled with euhedral blocky mega-quartz (Qtz-B) or chalcedony-spherulitic quartz (Qtz-C). Qtz-C is lining the solutional voids. Images under cross-polarized light. D) Heterolithic texture in unit B2, with sub-mm to mm-thick intercalations of clay and silt characterized by wavy-bedding. Image under parallel-polarized light. E) Marly dolostone with dolomicrite matrix and high content of terrigenous detrital grains composed of quartz and K-feldspar. Image under parallel-polarized light. F) Siltstone in the tempestite facies of unit B3. Siltstones have a high porosity at thin section scale and present disseminated iron oxides-hydroxides. Image under parallel-polarized light. G) Rudstone texture in unit B3 made of Intraclasts (highlighted in yellow) and detrital grains composed of quartz and K-feldspar. Image under parallel-polarized light. Label abbreviations: r-dol (relict dolomite), Qtz-V (quartz veins), Qtz-A (micro-crystalline chert), Qtz-B (euhedral blocky mega-quartz), Qtz-C (chalcedony), Kfs-cl (detrital K-feldspar clast), Qtz-cl (detrital quartz clast), Intra-cl (carbonate intraclasts). (For interpretation of the references to color in this figure legend, the reader is referred to the Web version of this article.)

The sub-horizontal galleries have a sub-elliptical or circular shape (Figs. 3C and 7B) with a stepping roof profile, which reflects the collapse of layers in the ceiling above the silicified unit B1. Dolostones and marls in unit B2 have a cm-thick crushed texture at the contact with the cave walls. The pavements are made up of collapsed layers from the overlying units and soft white powders composed of gypsum and minor amounts of iron oxides/hydroxides or guano-derived phosphates. Secondary phosphates and iron-manganese oxides/hydroxides have also been found as overgrowths on the host rock. Calcite speleothems from percolation/evaporation of meteoric water decorate the walls and pavements in different sites of the middle storey.

4.1.3. *Upper storey and doline entrance – unit C*

The upper part of the CCS, from the entrance at the surface down to a depth of approximately 31 m, is characterized by isolated and small sub-horizontal galleries (Fig. 3D) connected with the middle storey by inclined or vertical conduits developed along through-going fracture zones. These small and short galleries are hosted in cherty dolostone layers (Fig. 8A, B, 8C) made up of thin-to medium-thick intercalations of dolomicrites and highly silicified ooidal grainstones/wackestones (unit C) and heteroliths (unit B2) (Fig. 8C and D).

Unit C is composed of medium-to thick-layers of dolostones with mudstone texture (Fig. 8E) or ooidal wackestone/grainstone texture with low content of detrital grains. Micro-crystalline quartz replacements of dolomite grains and cement are common (Qtz-A) and frequently associated with the ooid-rich facies (Fig. 8F). Chalcedony (Qtz-C) or euhedral blocky mega-quartz (Qtz-B) filling vuggy pores and veins are also observed in this unit (Fig. 8D). Vuggy pores and veins in the upper part of unit C may also be filled with calcite crystals (Fig. 8E). Pressure solution by bedding parallel stylolites postdates the Qtz-A silicification episode both in thin-section and outcrop scale, causing apparent offsets and plastic deformation of chert nodules (Fig. 8B).

Above the heterolith intercalations, the cave morphology consists of collapse halls and small chambers connected with the surface by a collapse. The entrance has a gentle slope covered with debris, boulders, and red soil coming from the surface (Fig. 3E). The passages near the entrance present condensation-corrosion features.

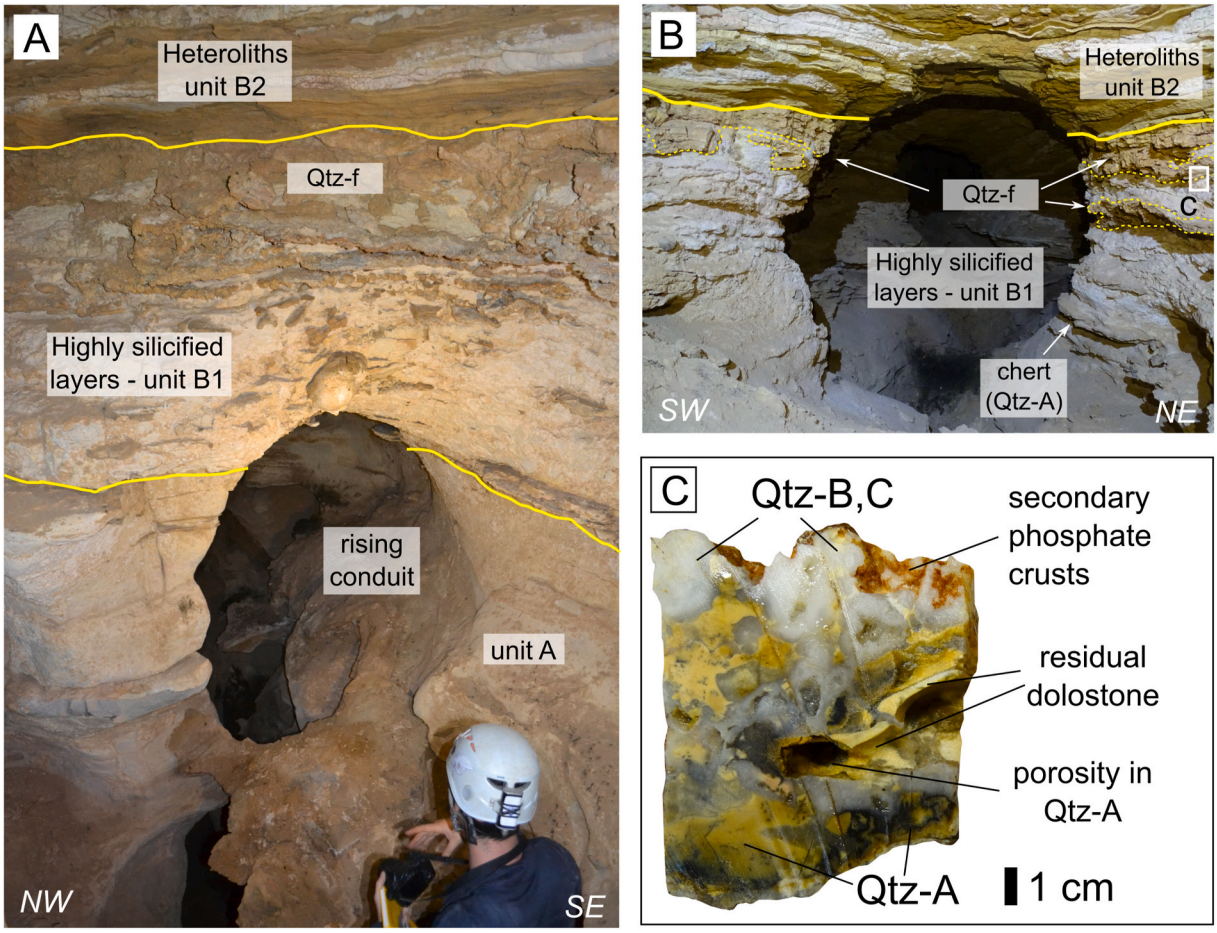

Fig. 7. A) Rising conduit localized in the dolomitized grainstones of unit A, at the top contact with units B1 and B2 where the middle storey (picture in box B) develops. Note the high concentration of quartz-rich mineral deposits in the upper part of unit B1. B) Sub-horizontal and rounded galleries in the middle storey. Galleries are organized in a maze network confined by units B2 and B3. Frequent collapses and evidence of dissolution by condensation-corrosion in the dolostone layers of units B2 and B3 contributed to the enlargement of the passages. C) Hand sample taken in the silicified unit B1 (location pointed in the picture in box B). Secondary guano-related phosphatic overgrowths (identified by SEM-EDS, Tab.1) form brown crusts on the mega-quartz crystals. Vuggy porosity (barren or filled) is concentrated in Qtz-A. Labels abbreviations: Qtz-f (undifferentiated quartz filling), Qtz-A (micro-crystalline chert), Qtz-B (euhedral blocky mega-quartz), Qtz-C (chalcedony). (For interpretation of the references to color in this figure legend, the reader is referred to the Web version of this article.)

4.2. Silicification textures

Quartz and silicified textures occur in all sedimentary units outcropping in the CCS. However, the highest concentration of silica and quartz-rich facies is observed in unit B1, associated with the sub-horizontal maze network of the middle storey (Fig. 7). Silicification occurs mainly as diagenetic replacement of dolomite grains and cement by micro-crystalline quartz (Qtz-A; Figs. 6A and 9). Qtz-A forms nodules and irregular layers, mainly localized in the dolomitized ooidal wackestone or mudstone textures and associated with small size (<20 μm) iron- and iron-titanium oxides or, less commonly, pyrite. The replacement process is shown by micron-sized ghosts of the precursor carbonates (Maliva and Siever, 1989). Ghosts resemble the typical rhombohedral dolomite grains and are mostly composed of fluid inclusions or microcavities that were not completely replaced by micro-crystalline quartz (Figs. 9B and 10B). At the meso-scale, different tones of chert (from light yellow to dark grey, Fig. 7C) reflect the amount of associated iron oxides, rhombohedral-shaped inclusions, grain size, and porosity.

Chert nodules are often characterized by high porosity textures (up to 10–15%), occasionally filled with euhedral mega-quartz (Qtz-B; Figs. 6B, 9A and 9E, 9F, 9G), chalcedony/spherulitic quartz (Qtz-C; Figs. 6B, 9E and 9F) or apatite (Fig. 10E). The contact between Qtz-A and Qtz-B/Qtz-C fillings is usually sharp with irregular rims (Fig. 9E and F). These mega-quartz and chalcedony deposits are characterized by several mineral inclusions illustrated in the SEM images of Fig. 10. Mineral inclusions in Qtz-B/Qtz-C are composed of Ca-sulfates (anhydrite and gypsum), barite, K-feldspar, Fe–Ti oxides and hydroxides, muscovite, apatite, and accessory Fe–Cr spinels (chromite group), sphalerite (very small crystals found in association with Ca-sulfates), and pyrite. Furthermore, Qtz-B occasionally displays colloform-plumose textures and undulose extinction.

Silicification expressed by Qtz-B and Qtz-C is mainly concentrated in the middle and lower storeys, below the heterolithic and tempestite facies of units B2 and B3. Quartz-filled veins are observed also in the upper storey, near faults and through-going FZ (Fig. 8D). Furthermore, mm-to cm-thick lenses of hydraulic breccias have been observed in thin sections from the middle storey (Fig. 9H, I, 10H). These hydraulic breccias are composed of sub-euhedral grains and fragments of quartz, K-feldspar, and phosphates (apatite, monazite; Fig. 10I) supported by a matrix of weathered host rock (mostly clay minerals and feldspars altered in muscovite, and pseudomorphs of hematite-goethite). Due to their small size and irregular textures, it was not possible to clearly establish if the REE-phosphates found in the alteration zones are relict detrital grains or authigenic.

The mineral list identified with SEM-EDS combined with petrographic analyses in the highly silicified unit B1 are summarized in Table 1.

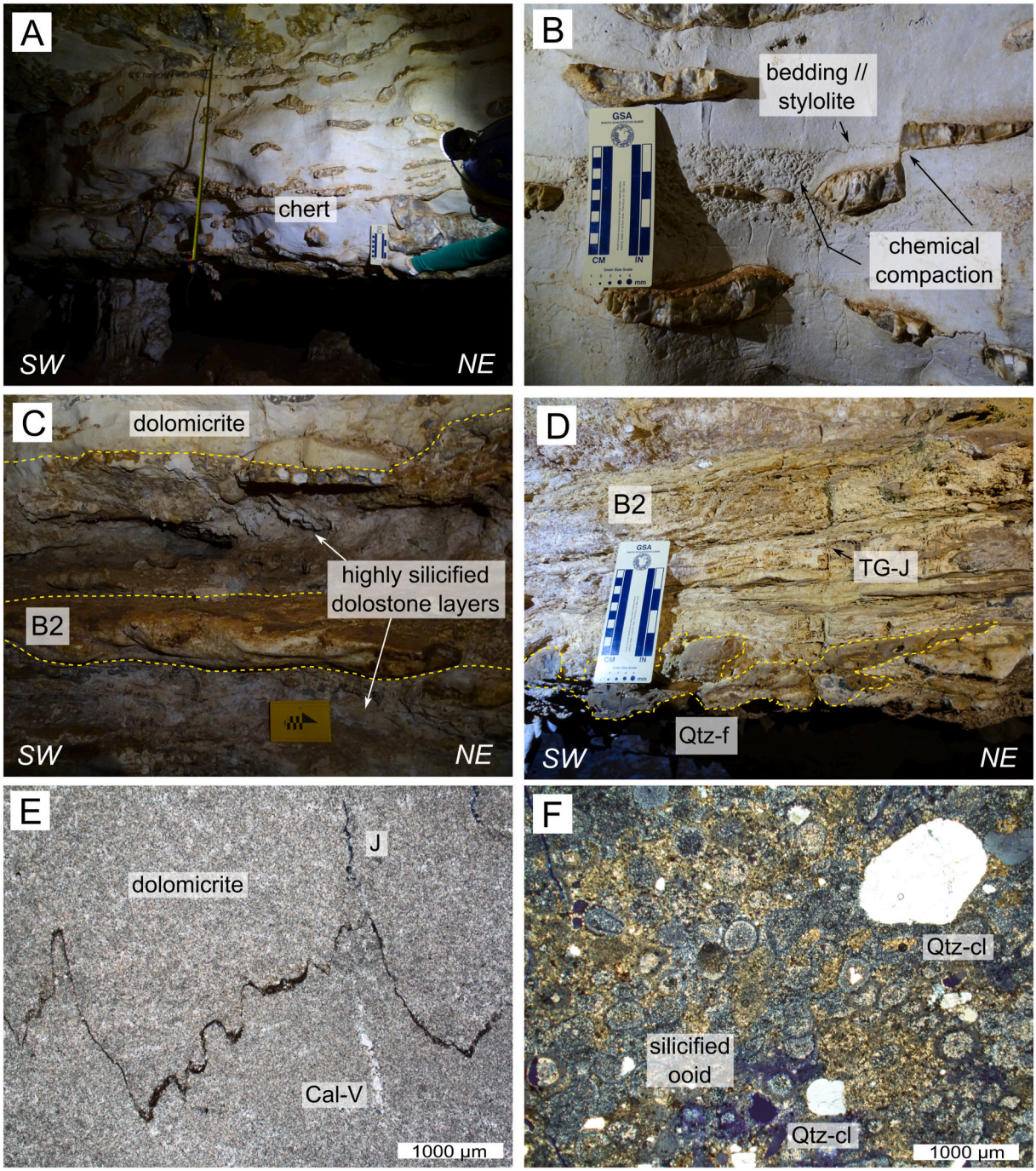

Fig. 8. Mesoscale (outcrop) and microscale (thin-section microphotographs) observations in unit C. A) Thick dolostone layer composed of dolomicrite (microphotograph in box E) with chert nodules. B) Close-up view of chert nodules deformed by bedding-parallel pressure solution (stylolites). Differential dissolution produced an apparent offset in the chert nodules, indicating that it postdates the formation of the chert nodules in the dolostone. C) Typical cave passage in the upper storey with the greatest widening localized in the cherty dolostone layers. D) Heterolith layers with wavy bedding and quartz-rich mineral deposits in unit B2. E) Dolomicrite with bedding-parallel stylolite in unit C. Image under parallel-polarized light. F) Silicified dolostone layer in the upper storey (see picture in box C) with ooidal grainstone texture and abundant detrital quartz grains. Silicification is represented by Qtz-A replacing dolomite grains and cement. Image under cross-polarized light. Label abbreviations: TG-J (through-going joint), J (joint), Qtz-f (mega-quartz filling porosity), Cal-V (calcite vein), Qtz-cl (quartz clast).

4.3. Deformation and fracture patterns

The structural elements observed in the CCS were classified as: stylolites, open-mode fractures (joints/veins), through-going fracture zones (FZ), and faults (Fig. 11A).

Bedding in the CCS is sub-horizontal to gently dipping to the NW (<5–15°) (Fig. 11B). Bedding-parallel stylolites due to burial were observed in all carbonate units and, especially, in units A and B1.

Open-mode fractures are joints and veins (Fig. 11B and C). Infilling of veins is made up of carbonates (mostly dolomite and calcite) or quartz. Boxwork quartz veins (Fig. 6B and C) are common in the lower and middle storey and are composed of Qtz-B or Qtz-C assemblages (Fig. 5C). Open-mode fractures are commonly bed-perpendicular or high angle to bedding, and either stratabound (confined to bedding interfaces) or shorter than single bed thickness. Based on the statistical analysis of fracture orientations, four sets of open-mode fractures were

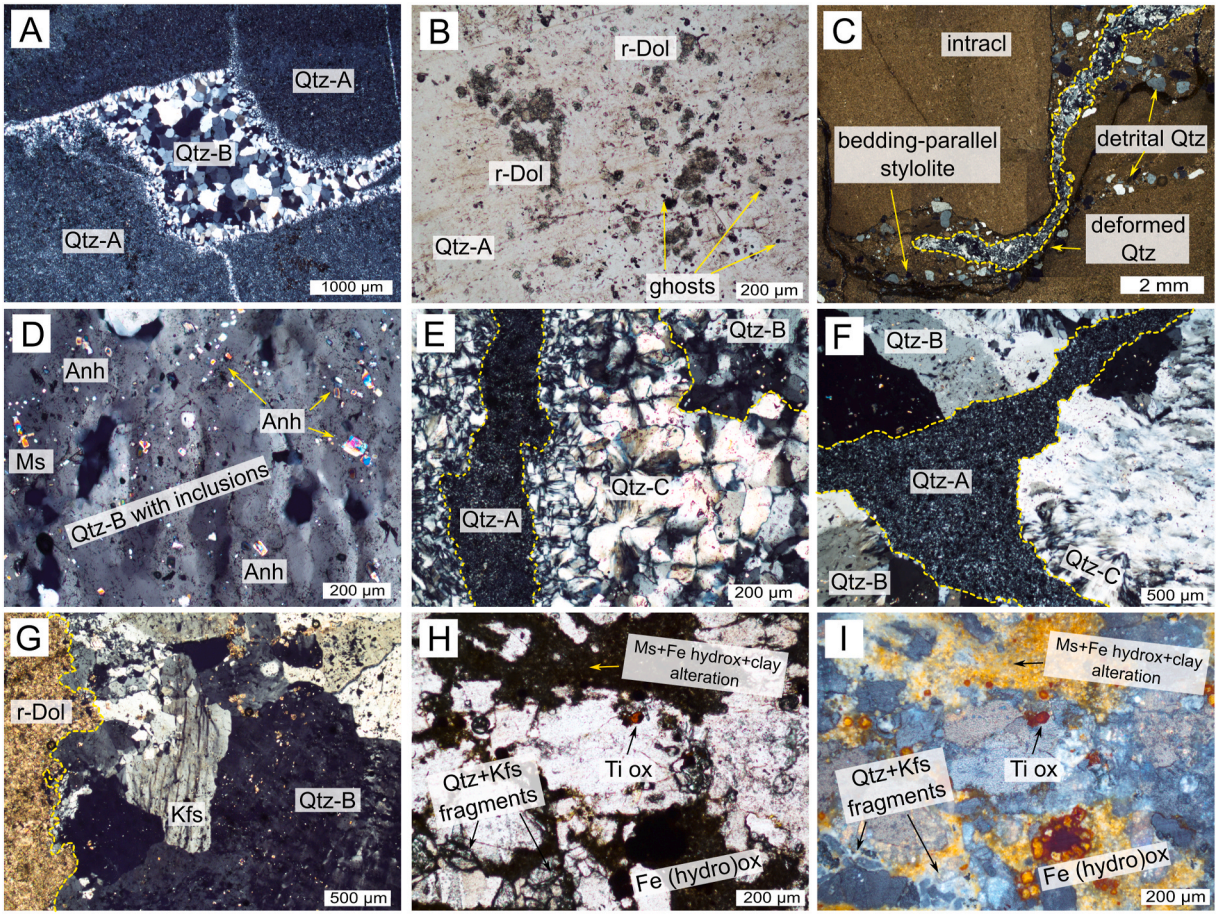

Fig. 9. Silicification microtextural observations at optical microscopy. A) Microcavity and veins in Qtz-A (chert) filled by euhedral blocky mega-quartz (Qtz-B). Image under cross-polarized light. B) Qtz-A replacing dolomite crystals. Ghosts of relict rhombohedral dolomite crystals are still visible. Image under parallel-polarized light. C) Mosaic of multiple microphotographs showing silicification features plastically deformed by bedding-parallel pressure solution in an intraclastic rudstone of unit B3. Images under cross-polarized light. D) Secondary mineral inclusions in a mega-quartz crystal (Qtz-B). Minerals with high interference colors are anhydrite, barite, or muscovite crystals. Image under cross-polarized light. E) Detail of spherulitic-chalcedony quartz (Qtz-C) and micro-crystalline quartz (Qtz-A). In the upper right corner, there are euhedral blocky quartz crystals (Qtz-B) with mineral inclusions. Image under cross-polarized light. F) Qtz-A with sharp rims and Qtz-B and Qtz-C crystallizations. Image under cross-polarized light. G) Association of Qtz-B with undulose extinction and K-feldspar with perthitic texture. On the left side, there are residual non-silicified dolomite crystals. Image under cross-polarized light. H) Micro-scale hydraulic breccia textures with quartz and K-feldspar fragments supported by a matrix composed of muscovite, iron-oxides/hydroxides, and altered clay or feldspar minerals. Images under parallel-polarized light. Quartz crystals have iron-titanium oxides inclusions. I) Same picture of box H under reflected light microscope with crossed nicols. Label abbreviations: Qtz-A (micro-crystalline quartz), Qtz-B (euhedral blocky mega-quartz), Qtz-C (chalcedony/spherulitic quartz), Qtz (quartz), Ms (muscovite), Anh (anhydrite; high interference colors), Kfs (K-feldspar), intracl (intraclasts), Fe (hydro)ox (iron-oxides and iron-hydroxides), Ti ox (titanium oxide, rutile), r-Dol (relict dolomite). (For interpretation of the references to color in this figure legend, the reader is referred to the Web version of this article.)

identified: NW-SE, N–S to NNE-SSW, NE-SW, and E-W (Fig. 11F). Non-stratabound (through-going) fracture zones (FZ), on the contrary, are formed by cm-spaced joints, veins, or sheared joints organized in connected arrays, which cut across bedding (Fig. 11D). Through-going FZ include NW-SE and N–S to NNE-SSW sets (Fig. 11G). These structures are mostly developed in the lower storey (unit A).

The dolomitized grainstones in unit A are also affected by rare small-scale faults (Fig. 11E) interpreted as sheared through-going fracture zones (Myers and Aydin, 2004), which display similar characteristics and orientation to the previously mentioned FZ sets. In these faults, kinematic indicators are rarely observed, so that slip sense is generally evinced from the vertical throw of bedding interfaces or bedding-parallel stylolites. These small-offset (<1 m) faults have oblique-slip kinematics: right-lateral on the NW-SE trend and left-lateral on the NNE-SSW trend (Fig. 11A and E). Furthermore, secondary E-W-striking low angle reverse faults are observed; they cause small-scale detachments (throws up to 1–5 cm) of heterolith layers in the middle storey.

Fracture properties of open mode stratabound fractures measured along linear scanline are shown in Table 2.

NW-SE, N–S, and NE-SW sets were measured in unit A. The NW-SE set shows a mean fracture spacing of 65–66 mm and a Cv value of 1.07. The N–S set has a mean spacing of 29–30 mm and a Cv value of 0.73. Finally, the NE-SW set shows a mean spacing of 56–57 mm and a Cv value of 0.56. In unit A, NW-SE and N–S through-going FZ were encountered along the linear scanlines; their real properties, however, were not measured due to the intense karst weathering.

The highly silicified layers in unit B1 (middle storey) show a high intensity of stratabound fractures (P_{10} ranging from 30 to 37 m^{-1}) with respect to the surrounding carbonate layers. Two main joint sets were recognized: NW-SE, with a mean spacing of 12–13 mm, and N–S, with a mean spacing of 52–53 mm. The Cv values are respectively 1.29 and 0.68. These two closely spaced fracture sets are organized in well-connected clusters.

In the scanlines through the marly dolostones and mudstones of unit B2, three main sets of stratabound open-mode fractures were identified: NW-SE, NE-SW and E-W. The NW-SE set shows a mean fracture spacing of 92–93 mm and a Cv value of 0.71. The NE-SW set has a mean spacing

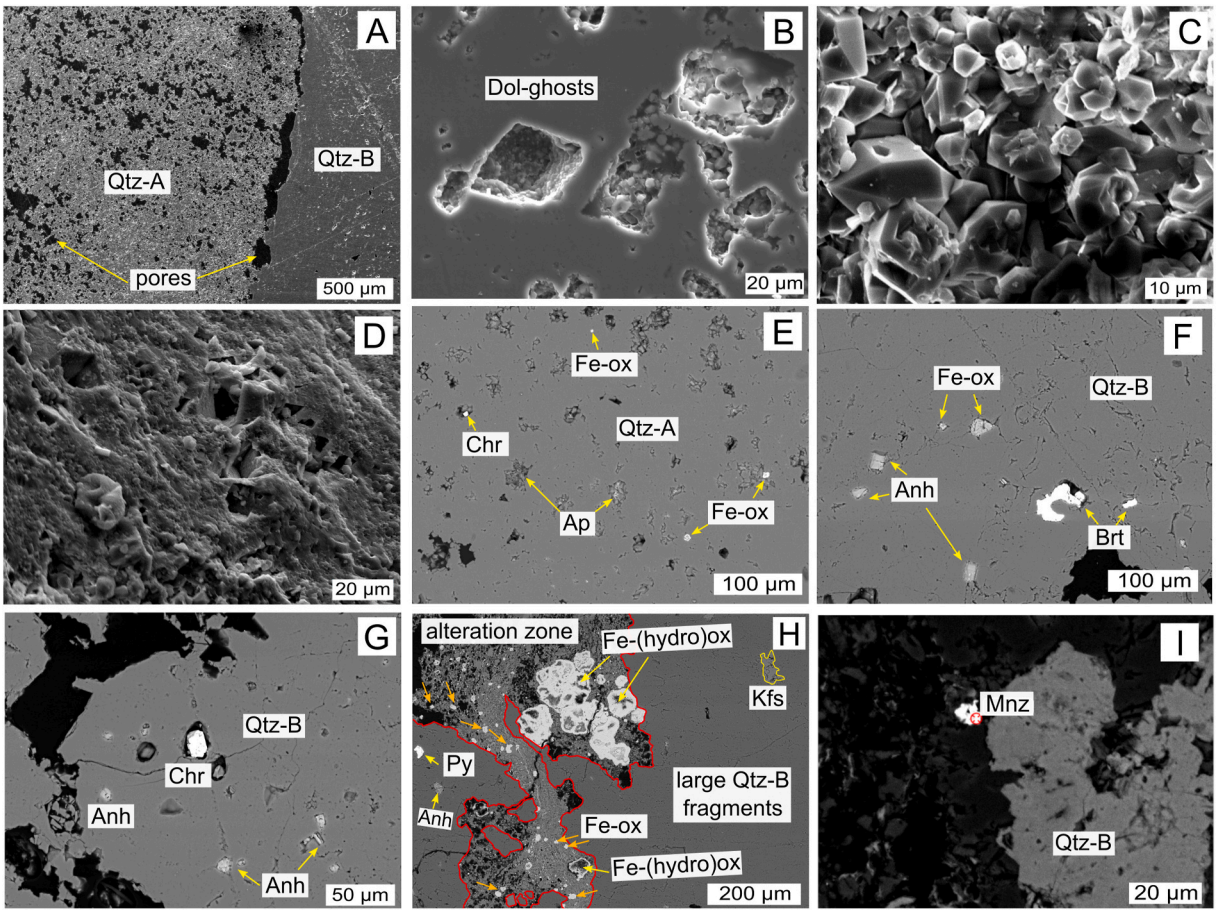

Fig. 10. Silicification micro-textures observed at SEM. A) Contact between Qtz-A and Qtz-B. Note the vuggy and intercrystalline porosity (~15–20%) in the Qtz-A texture. B) Rhombohedral-shaped dolomite ghost inclusions in Qtz-A. C-D) Micro-textures typical of slow dissolution kinetics (Mecchia et al., 2019) in Qtz-A, like: "V"-shaped notches, corrosion holes and etch pits. E) Qtz-A associated with iron-oxide crystals and intercrystalline voids filled with Fe–Cr spinel and apatite crystals. F) Qtz-B with inclusions of anhydrite, iron oxides, and barite crystals. G) Qtz-B with inclusions of Fe–Cr spinel and sulfates (mostly anhydrite). H) Hydraulic breccia micro-texture with associated alteration zone in a heterolith layer of unit B2. The orange arrows point to iron oxide-hydroxide aggregates disseminated in the alteration zone. I) REE (Ce, La, Nd, Th)-phosphate (monazite) in the hydraulic breccia alteration zone. From A to D: SE images; from E to L: BSE images. Label abbreviations: Qtz-A (micro-crystalline quartz), Qtz-B (euhedral blocky mega-quartz), Qtz (quartz), Kfs (K-feldspar), Anh (anhydrite), Brt (barite), Py (pyrite), Chr (Fe–Cr spinel group), Fe-ox (iron oxides), Fe-(hydro)ox (iron-oxides and iron-hydroxides), Ap (apatite), Mnz (REE-phosphate, monazite). (For interpretation of the references to color in this figure legend, the reader is referred to the Web version of this article.)

of 129–130 mm, and a Cv value of 0.42. Finally, the E-W set shows a mean spacing of 22–23 mm, and a Cv value of 0.7.

In the tempestite facies of unit B3, a minor intensity of brittle deformation (P_{10} ranging from 3.7 to 4.7 m^{-1}) is observed with two main joint sets striking NW-SE and NE-SW. Both sets show mean spacing around 20–21 cm and Cv values of 0.47 and 0.52, respectively.

In unit C, scanlines were measured both on chert nodules and carbonate layers (dolomicrite). The main sets measured are NW-SE and N–S. In the dolomicrite layer, the NW-SE set shows a mean spacing of 95–96 mm and a Cv value of 1.43, whereas the N–S set shows a mean spacing of 51–52 mm and a Cv value of 0.79. The NW-SE and N–S joint sets in the chert nodules result respectively in mean fracture spacing of 53–54 mm and 16–17 mm, and Cv values of 1.01 and 0.97, respectively.

The silicified and cherty dolostone facies show the closest-spaced fracture sets, as well as the highest degree of fracture connectivity noticed by field observations both in map (Fig. 12A) and section view (Fig. 12B). On the contrary, in the carbonate-dominant and siliciclastic facies (Fig. 12C and D) fractures are mainly constituted of stratabound veins with variable apertures and wide spacing. In the lower storey, localization of through-going FZ and faults can produce volumes of channelized fracture permeability testified by their association with feeders (Fig. 5B and C), rising conduits (Fig. 7A), and karst development (Fig. 11D). The fracture intensity (P_{10}) was calculated for each scanline and is reported in Fig. 12E and Table 2.

4.4. Petrophysical properties

The fracture properties collected from different scanlines in the cave allowed to characterize the variations in fracture normal spacing and to estimate individual fracture permeability for the whole sedimentary sequence outcropping in the CCS (Philipp et al., 2013; Giuffrida et al., 2020). The results are displayed in $\log_{10}$ scale as box-plot diagrams (Fig. 13), subdivided by fracture sets and grouped according to the different sedimentary units described in the previous sections. The crosses in the boxplots refer to mean values, whereas the left and right box sides are the 1st and 3rd quartiles, respectively. The box whiskers define the minimum and maximum values in the data range excluding outliers. Estimated individual fracture permeability in unit A ranges from 10^3 to 10^5 mD, with a mean value around 10^4 mD. In unit B1, stratabound fractures are closely spaced (mean values around 10^1 mm), and they have a fracture permeability with mean values between 10^4 and 10^5 mD for each individual set. Unit B2 has variable permeability values, with means around 10^3 mD. In the siltstones of unit B3, fracture spacing is wide (up to 10^2–10^3 mm) and the mean fracture permeability is around 10^4–10^5 mD. Finally, in unit C fracture permeability is higher in the silicified zones with chert nodules (means between 10^2 and 10^3

Table 1
List of the mineral phases associated with silicification identified by combined SEM-EDS and petrographic microscopy.

Name	Simplified formula	Description
Quartz	SiO_2	microcrystalline (Qtz-A) chert as diagenetic replacement of dolomite; blocky mega-quartz (Qtz-B) or chalcedony (Qtz-C) filling porosity and fractures; fragments in hydraulic breccias
Hematite	Fe_2O_3	pseudomorphs of pyrite; associated with silicification and hydraulic breccias; inclusions in hydrothermal quartz; overgrowths and coatings
Pyrite	FeS_2	disseminated in dolomitized carbonate, mainly replaced by hematite-goethite; inclusions in hydrothermal quartz
Sphalerite	ZnS	rare inclusions in hydrothermal quartz
Goethite	FeO(OH)	alteration of hematite crystals; coatings
Pyrolusite	MnO_2	alteration of bedrock
Gypsum	$CaSO_4 \cdot 2H_2O$	lamellar gypsum filling porosity and as overgrowths; soft powders on cave floors; inclusions in hydrothermal quartz
Anhydrite	$CaSO_4$	inclusions in hydrothermal quartz
Barite	$BaSO_4$	inclusions in hydrothermal quartz
K-feldspar	$K(AlSi_3O_8)$	inclusions in hydrothermal quartz and filling pores; fragments in hydraulic breccias
Muscovite	$KAl_2(AlSi_3O_{10})(OH)_2$	inclusions in hydrothermal quartz; alteration zones associated with hydraulic breccias
Calcite	$CaCO_3$	vein fillings
Dolomite	$CaMg(CO_3)_2$	primary dolomitization of calcite grains and cement
Montmorillonite	$(Na,Ca)_{0.33}(Al,Mg)_2(Si_4O_{10})(OH)_2 \cdot nH_2O$	residual clay minerals in bedrock
Taranakite	$K_3Al_5(PO_3OH)_6(PO_4)_2 \cdot 18H_2O$	crusts on cave walls and overgrowths on quartz deposits, guano-related phosphates
Robertsite-Mitridatite series	$Ca_2(Mn^{3+},Fe^{3+})_3O_2(PO_4)_3 \cdot 3H_2O$	crusts on cave walls and overgrowths on quartz deposits, guano-related phosphates
Brushite	$Ca(PO_3OH) \cdot 2H_2O$	crusts and acicular overgrowths on quartz deposits, guano-related phosphates
Apatite	$Ca_5(PO_4)_3(OH)$	inclusions in hydrothermal quartz deposits and filling pores, or guano-related overgrowths on quartz deposits
Berlinite-Variscite group (?)	$Al(PO_4) - Al(PO_4) \cdot 2H_2O$	guano-related phosphates
Hematite-Ilmenite series	Fe_2O_3 - $FeTiO_3$	inclusions in hydrothermal quartz
Rutile	TiO_2	inclusions in hydrothermal quartz
Chromite group	$FeCr_2O_4$	inclusions in hydrothermal quartz
REE-phosphates (Monazite Group)	REE (PO_4)	small grains in the alteration zones of hydraulic breccias or detrital (?)
Ni-phosphate (?)	?	small grains in the alteration zones of hydraulic breccias or detrital (?)

mD) than in the dolomicrite facies (means between 10° and 10^{1} mD).

On the right side of Fig. 13, the rock plug measurements of porosity (expressed in %) and permeability (expressed in mD) are displayed in a $\log_{10}$ scale. Rock plug permeability values are subdivided into horizontal and vertical permeability. The colored dots represent the mean values, whereas the whiskers refer to the 1st and 3rd quartiles of the datasets. The results from the analyses are displayed in a $\log_{10}$-$\log_{10}$ diagram in Fig. 14, where trendlines represent the best fit power-law distribution of the datasets subdivided by sedimentary units. All R^2 values are >0.7 except in the silicified unit B1, where alteration and karst dissolution are intense and permeability values are scattered (R^2 value is 0.48). The mean R^2 value (R^2=0.72) of the trendlines confirms a good fit of the power-law distribution for the datasets.

Fig. 13 graphically describes the variations of petrophysical properties relative to the CCS lithostratigraphic profile and the spatial organization (pattern) of the hypogene conduit system. Rocks in unit A have low-medium porosity (ranging from 2% to 15%, mean value of 6%) and permeability values range from 10^{-3} to 10^{2} mD (maximum 129.1 mD). The silicified unit B1 presents medium porosity (from 5% to 16%, with a mean of 11%) and variable permeability with values ranging from 10^{-2} to 10^{3} mD (maximum 231.7 mD in bedding-parallel plugs). The heterolithic and tempestite facies of units B2 and B3 have the highest porosity values, ranging from 6% to 29%, with mean values respectively of 11% and 20%. On the other hand, the permeability of rock plugs is low, with values ranging from 10^{-3} to 10^{1} mD. In unit C, values of porosity are significantly different between the rocks in the upper speleogenetic storey (mean value of 6%) and those from the passages comprised between the entrance and the intercalations of unit B2. The latter have the lowest porosity of the entire dataset (1–2%). In a similar way, the permeability of rock plugs has low values around 10^{-3} mD in the upper interval of unit C, and variable values ranging from 10^{-3} to 10^{1} mD in the karstified upper storey.

EPM permeabilities for each speleogenetic unit in the CCS, calculated for discharge parallel to the main fracture sets (K_P) or normal to the main fracture sets (K_N), are summarized in Table 3. These values reflect the anisotropy in permeability for the different speleogenetic units in the CCS.

5. Discussion

This study provides evidence for hypogene flow and karst dissolution in a silicified carbonate-siliciclastic sequence. Our observations allow us to propose a conceptual evolutionary model for the CCS, identifying different fluid flow pathways and hypogene speleogenetic mechanisms that drastically modified the original porosity-permeability of the layered sedimentary sequence. Furthermore, the CCS represents a conceptual analog of many deep carbonate reservoirs where silicification and hydrothermal alteration are common processes making the characterization of the reservoir properties a challenging task (De Luca et al., 2017; Montanari et al., 2017; Lima et al., 2020). In particular, the pre-salt carbonate reservoirs of Campos Basin (Lima et al., 2020) and Kwanza Basin (Poros et al., 2017) show silicification and dissolution features similar to those documented in the CCS.

In the next sections, we discuss the role of structural-stratigraphic variability in the definition of high vs. low permeability zones, hypogene fluid migration, and dissolution. Our observations are integrated into conceptual models illustrating the spatial-temporal evolution of the sequence and its implications for karst reservoirs.

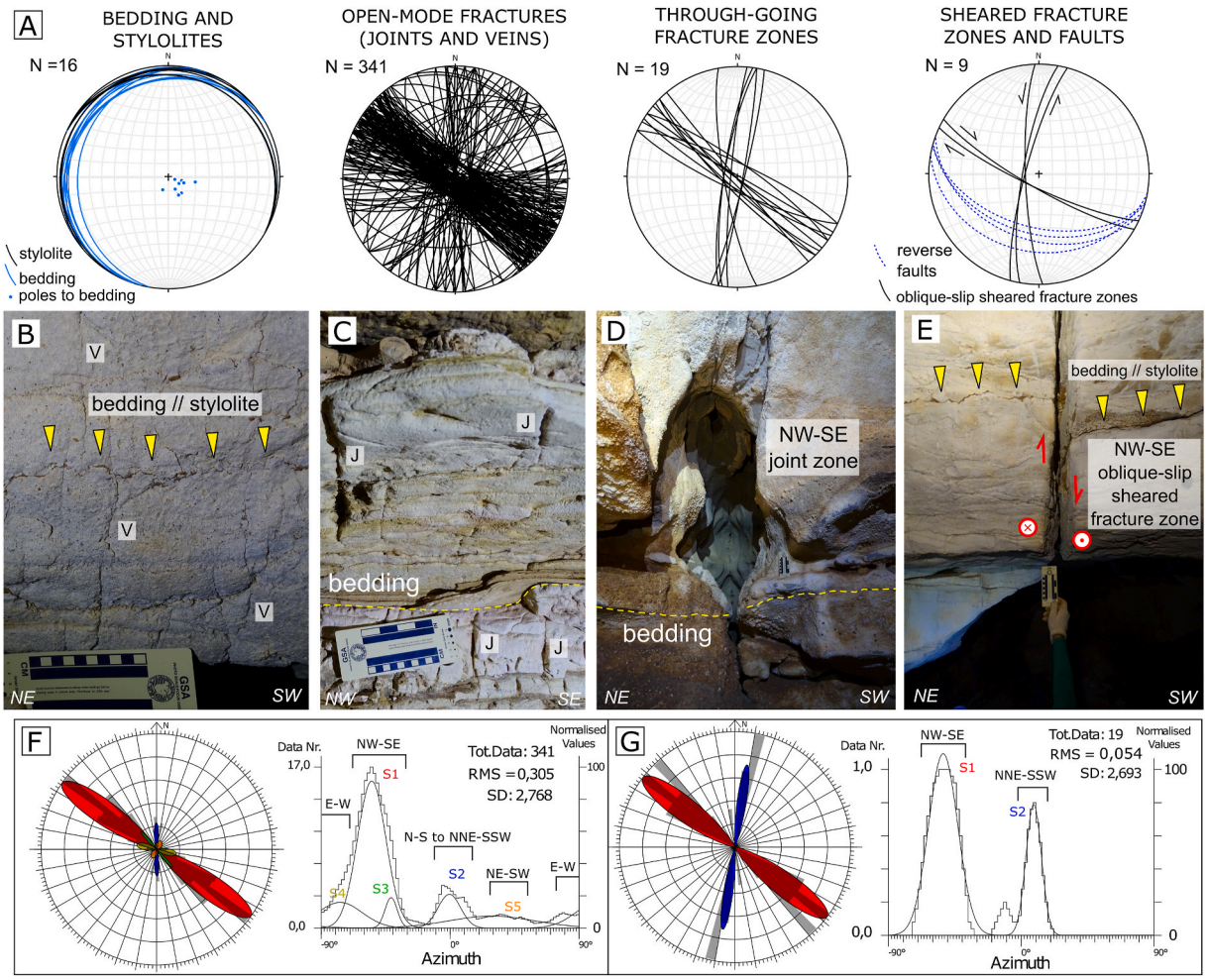

Fig. 11. A) Structural features measured in the CCS displayed with lower-hemisphere equal-area stereographic projections and classified by type. B) Example of bedding-parallel stylolites and stratabound veins in the dolostones of unit A. C) Example of open-mode stratabound fractures (joints) in the dolomicrites and marly dolostones of unit B2. D) Karst dissolution along a through-going FZ composed of clustered open-mode fractures (joints) in unit A. E) Example of a small-scale fault along a NW-SE through-going fracture zone reactivated in shear (oblique-slip). F-G) Statistical analysis by Gaussian-best fit calculated from the normalized frequency distribution histograms for both the open-mode fracture dataset (F) and the through-going FZ dataset (G). Azimuth data are given in ±90°. RMS: root mean square error; SD: standard deviation.

5.1. High permeability vs. seal (buffering) units, fluid flow pathways, and hypogene dissolution

Permeability pathways and karst formation in fractured and layered carbonates mostly depend on the interaction between stratigraphy, fracture patterns, diagenetic features, and the hydrogeological-speleogenetic setting (Audra and Palmer, 2015; Klimchouk, 2019; Balsamo et al., 2020). The recognition of the main hydrological behavior of the sedimentary units composing a layered sequence is therefore fundamental to correctly interpret its speleogenetic evolution in space and time (Klimchouk, 2007; Klimchouk et al., 2009).

The analyses of fracture patterns, petrophysical properties, and speleogenetic features in the different sedimentary units of the CCS allowed to recognize high permeability and "seal" (buffering) units (Table 3; Fig. 13). These hydrogeological-speleogenetic units strongly influenced fluid flow directions and resultant karst geometries. Due to the limited scale of observation and the lack of regional data, we define these "seal" units as low permeability buffer zones. Such zones vary in lateral thickness and might be breached by non-stratabound fractures (Fig. 11). These vertically extended fractures act as conduits in specific discharge areas of the regional groundwater system (Klimchouk et al., 2016).

Based on the field analyses, microtextural observations and analytical results presented in the previous sections, we propose a timeline for the main diagenetic, structural and speleogenetic phases that affected the CCS sequence. The spatial-temporal evolution is illustrated in the conceptual model of Fig. 15. In the following sections, we refer to three main diagenetic evolution stages as defined by Choquette and Pray (1970) and Morad et al. (2000): eodiagenesis, corresponding to the early processes taking place at shallow depth near the surface (commonly up to a few hundred meters below the surface); mesodiagenesis, corresponding to the burial interval below the influence of near-surface processes until the onset of low-grade metamorphism; and telodiagenesis, corresponding to the processes that take place during uplift and exhumation of previously buried rocks.

5.1.1. Stages 1 and 2 – early diagenetic silicification and burial

Silicification in the CCS affected selected carbonate layers; in some of these layers (unit B1) SiO_2 content can reach up to 80-85 wt% (Fig. 4). The main episode of diffuse silicification is represented by the formation of chert nodules. Micro-crystalline quartz (Qtz-A) replaces the carbonate grains and cement and forms nodular aggregates (Figs. 6, 9 and 10).

The precursor carbonate units in the CCS are entirely composed of dolostones. Almost no calcite has been found, although several fabric characteristics and microtextures (like ooids) are still preserved in thin sections indicating original calcite deposition. Since it is not the focus of

Table 2
Scanline properties and quantitative fracture attributes measured for the open-mode fracture sets identified in the CCS.

	Scanlines properties						
Sedimentary unit	Study site	Lithology	Scanline trend	Scanline length (m)	Layer thickness	n	Linear intensity P_{10} (m^{-1})
A	point H	Crystalline dolostone	N12E	0.8	36 cm	15	18.75
	point A	Crystalline dolostone	N120E	0.75	41 cm	14	18.67
B1	point G	Highly silicified dolostone	N50E	0.35	8 cm	13	37.14
	point F	Highly silicified dolostone	N107E	0.9	6 cm	27	30.00
B2	point F	Marly dolostone	N107E	1.8	8 cm	19	10.55
	point G	Dolomicrite	N50E	0.8	10 cm	15	18.75
	point G	Marly dolostone	N50E	1.4	18 cm	9	6.43
B3	point F	Coarse laminated siltstone	N90E	3	20 cm	11	3.67
	point G	Mixed carbonate-siliciclastic coarse sandstone	N40E	3	36 cm	14	4.67
C	point J	Dolomicrite	N120E	0.6	28 cm	8	13.33
	point J	Dolomicrite	N35E	1.8	100 cm	18	10.00
C (chert)	point J	Silicified cherty dolostone	N35E	0.5	9 cm	23	46.00

	Structural analysis					
Sedimentary unit	Fracture Set, Strike	Type of fractures	Mean normal spacing (mm)	Cv	Mean mechanic aperture (mm)	Mean hydraulic aperture (mm)
A	NW-SE, N122E	Stratabound joints/veins	65.67 ± 0.51	1.07	1.06 ± 0.74	0.053 ± 0.072
	N–S, N177E	Stratabound joints/veins	29.71 ± 0.31	0.73	0.48 ± 0.27	0.010 ± 0.011
	NE-SW, N33E	Stratabound joints/veins	56.92 ± 0.22	0.56	0.92 ± 0.60	0.037 ± 0.054
	N–S, N2E	Fracture zones (n = 2)	–	–	–	–
	NW-SE, N128E	Fracture zones (n = 9)	–	–	–	–
B1	NW-SE, N118E	Stratabound joints	12.92 ± 0.41	1.29	0.31 ± 0.12	0.042 ± 0.038
	N–S, N12E	Stratabound joints	53.19 ± 0.35	0.68	0.46 ± 0.15	0.043 ± 0.039
B2	NW-SE, N130E	Stratabound joints/veins	92.38 ± 0.26	0.71	0.56 ± 0.29	0.016 ± 0.019
	NE-SW, N55E	Stratabound joints/veins	129.86 ± 0.20	0.42	0.71 ± 0.35	0.005 ± 0.004
	E-W, N94E	Stratabound joints/veins	22.94 ± 0.41	0.70	0.73 ± 0.35	0.004 ± 0.002
B3	NW-SE, N131E	Stratabound joints	210.8 ± 0.24	0.47	1.16 ± 0.56	0.029 ± 0.030
	NE-SW, N21E	Stratabound joints	196.05 ± 0.21	0.52	0.9 ± 0.30	0.028 ± 0.017
C	NW-SE, N134E	Stratabound joints/veins	95.28 ± 0.54	1.43	0.15 ± 0.11	0.001 ± 0.001
	N–S, N4E	Stratabound joints/veins	51.35 ± 0.31	0.79	0.17 ± 0.08	0.001 ± 0.001
C (chert)	NW-SE, N128E	Stratabound joints	53.92 ± 0.45	1.01	0.08 ± 0.03	0.003 ± 0.001
	N–S, N178E	Stratabound joints	16.76 ± 0.38	0.97	0.09 ± 0.03	0.003 ± 0.002

this work, we will not discuss the dolomitization process. However, we hypothesize that the dolomitization should have occurred during eodiagenesis before the formation of chert nodules and after the diagenetic cementation of the original carbonate sediments.

From meso-to microscopic observations, the chert nodules in the carbonates predate pressure solution caused by burial (Figs. 8B and 9C), which developed at a depth generally <800–900 m (Van Golf-Racht, 1982; Rolland et al., 2014; Araújo et al., 2021). Furthermore, burial-related stylolites are common features consistent with eodiagenetic to early-mesodiagenetic settings (Caracciolo et al., 2014; Souza et al., 2021). We suggest, therefore, that the diffuse dolomite replacement and the formation of the chert nodules was likely restricted to shallow burial conditions and early diagenetic settings (<1 km: Fig. 15). The sources of Si-rich fluids which could have triggered this diffuse silicification, common also in other carbonates of the Salitre *Fm*, are still unknown. The hypothesis of hydrothermal solutions rising through the underlying Chapada Diamantina quartzites along basement-rooted structures has been suggested by some authors (Bertotti et al., 2020; Cazarin et al., 2021).

Mechanical compaction during progressive burial until the transition to early-mesodiagenesis caused open-mode regularly spaced fractures represented by the NE-SW and NW-SE striking sets (Fig. 11A; Table 2). Fracture localization in layers with high concentration of stiff chert nodules (unit B1) forms highly-connected joint networks (Fig. 12A and B).

5.1.2. Stage 3 – rising flow and deep-seated silica dissolution

Chert nodules in the CCS show a porous texture (Figs. 7C and 10A) and single quartz grains characterized by solutional pits, "V"-shaped notches, and dissolution related vugs (Fig. 10C and D; Higgs, 1979; Burley and Kantorowicz, 1986; Shanmugan and Higgins, 1988; Sauro et al., 2014; Itamiya et al., 2019). Dissolution features at different scales (Figs. 7 and 10), blocky mega-quartz and chalcedony filling solutional pores and fractures, and quartz-rich brecciated micro-textures suggest a complex history of fluid-rock interaction and mineralization during mesodiagenesis.

The widespread evidence of silica dissolution observed at the micro-scale in the CCS is particularly relevant for its implications regarding deep carbonate reservoirs. It is commonly known that quartz solubility exponentially increases with temperature (Siever, 1962; Rimstidt, 1997; Dove, 1999; Gunnarsson and Arnórsson, 2000; Marin-Carbonne et al., 2014; Sauro et al., 2014; Cui et al., 2017). Furthermore, silica solubility is nearly constant at pH<8, and significantly increases at greater values (Mitsiuk, 1974; Andreychouk et al., 2009; Mecchia et al., 2019). Also, Ba^{2+} transported in solution (suggested by the presence of barite mineralization in the CCS) could have determined a significant positive effect on quartz solubility, as reported by previous works (Dove and Nix, 1997; Sauro et al., 2014; Mecchia et al., 2019).

We propose that an early phase of hypogene dissolution occurred in deep-seated conditions, where silica-dominant dissolution was driven by warm (likely >100–150 °C) and alkaline fluids able to reach the silicified layers. The result was the formation of micro-scale karst (vuggy) porosity and solutionally-enlarged fractures in the cherts (Fig. 15). Mineral phases such as Fe–Cr spinels, Fe–Ti oxides, barite, anhydrite, sulfides, rutile, and phosphates (mainly apatite) found as solid inclusions associated with quartz mineralizations (Figs. 9 and 10; Table 1) strongly support a hydrothermal origin for this deep-seated hypogene phase.

Mechanical compaction during progressive burial and multiple tectonic events at the time of the *Brasiliano* Orogeny caused the formation of many different permeable structures (Fig. 11). Driven by pressure gradient and/or fluid buoyancy, the permeable structures focused upward flow, as suggested by the presence of the solutionally-enlarged feeders in the lower storey of the cave.

Our structural data indicate two main contractional events that postdate burial. The E-W striking open-mode fracture set is consistent

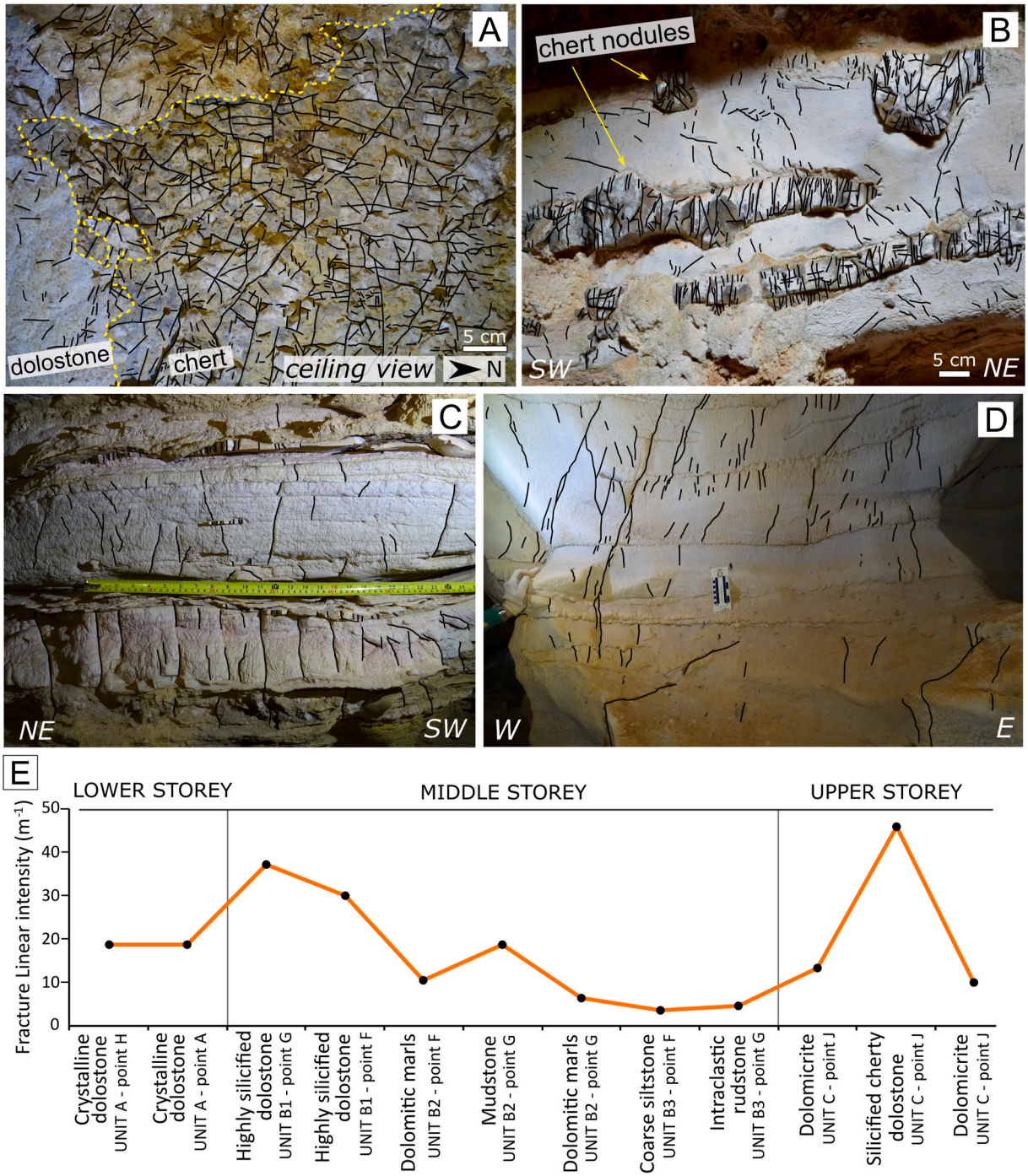

Fig. 12. Fracture patterns highlighted by line drawing in the different sedimentary units of the CCS. A) Example of fracture development in dolostone (low connectivity, low fracture density) and chert (high connectivity, high fracture density) in the highly silicified layers of the middle storey. Note that the picture represents a planimetric view of the ceiling. B) Different fracture patterns in the cherty dolomicrites of unit C (upper storey). Chert nodules localize brittle deformation and fracturing. C) Example of widely spaced and stratabound fractures in unit B2 (middle storey). Occasional through-going but poorly connected fractures are observed. D) Stratabound and clustered through-going fractures in unit A (lower storey). E) Fracture linear intensity (P_{10}) calculated for each scanline. Chert nodules in the highly silicified layers localize the highest values of P_{10} (30-40 m^{-1}).

with the first contractional phase (~E-W direction of maximum shortening) recorded also in other areas of the Una-Utinga basin (D'Angelo et al., 2019; Pontes et al., 2021). The second contractional event is related to the formation of the N–S to NNE-SSW open-mode fracture sets formed parallel to a roughly NNE-SSW direction of maximum shortening. Progressive deformation during this contractional phase produced the clustering of NNE-SSW joints/veins with the formation of through-going FZ in unit A. Based on our structural analysis, we propose that the same NNE-SSW contractional phase also controlled the reactivation of the pre-existent NW-SE joints/veins sets, causing the formation of clustered FZ eventually reactivated in shear (Myers and Aydin, 2004) with oblique-slip kinematics (Fig. 11E). These vertical structures acted as the main permeability pathways for rising fluid flow (Fig. 5B). Bedding-parallel NNE-SSW-oriented shortening also caused the formation of ESE-WNW small-scale reverse faults observed in the middle storey (Fig. 11A).

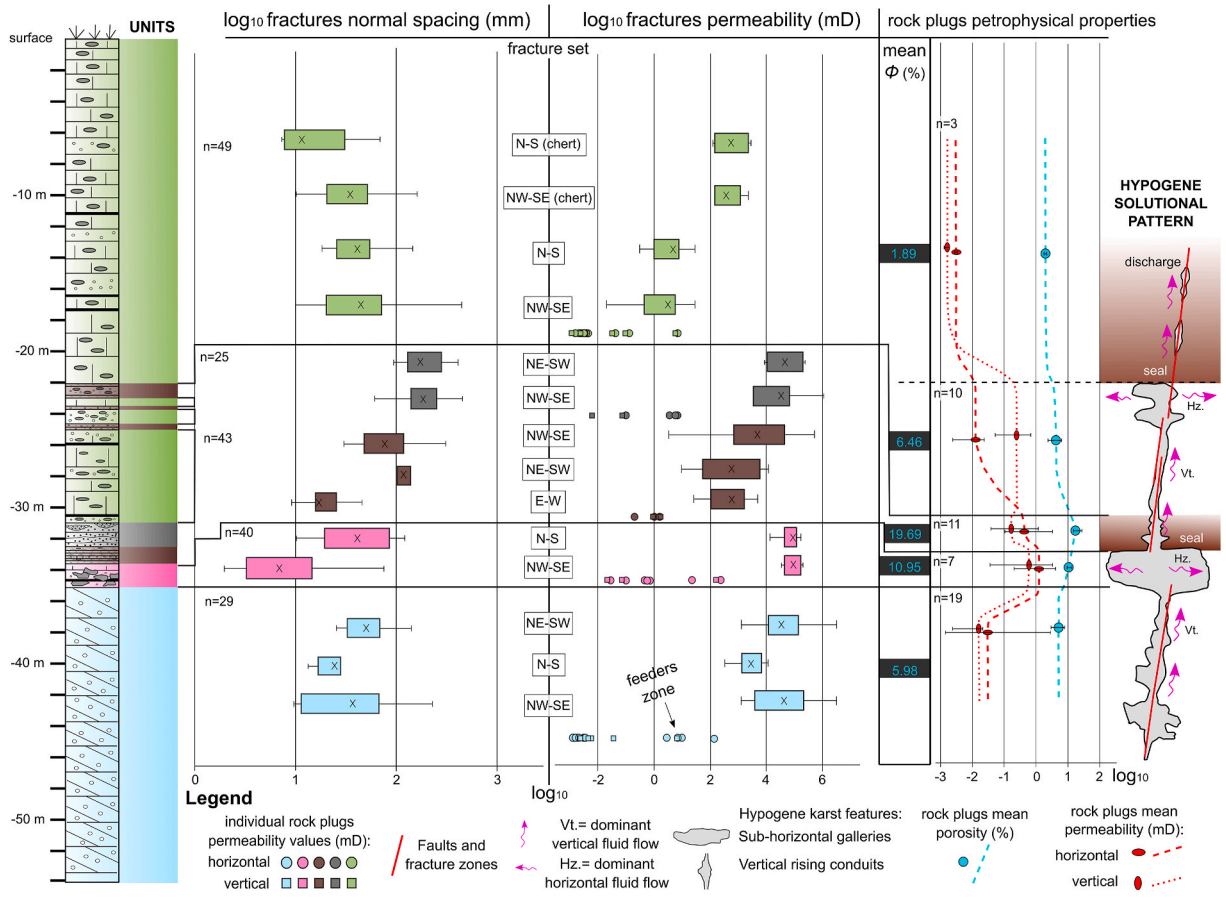

Fig. 13. Boxplots show the variation of petrophysical properties, fracture normal spacing, and fracture permeability of individual sets along the lithostratigraphic profile in the CCS gallery-conduit system. For the legend of the lithostratigraphic log, the reader is referred to Fig. 3.

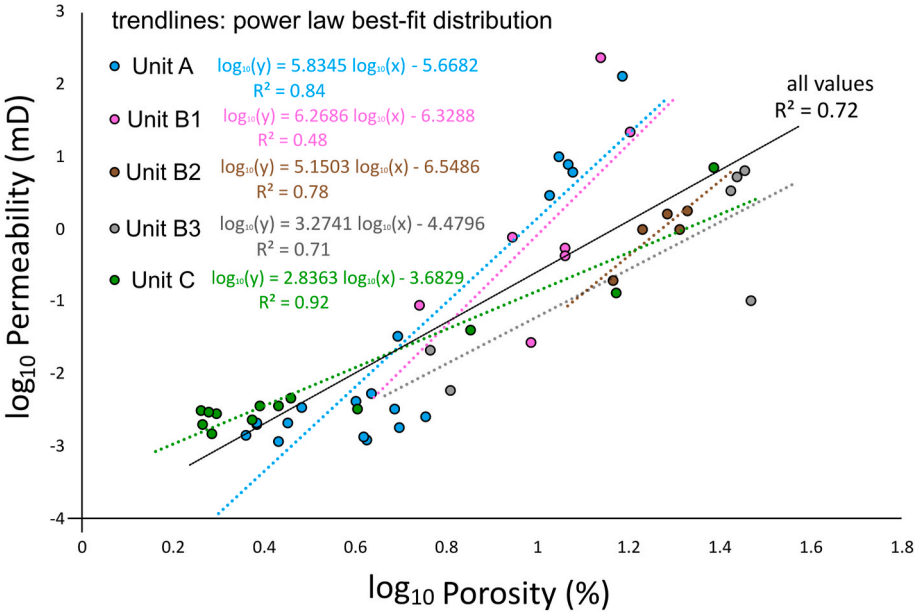

Fig. 14. Log-log diagrams showing the relationship between rock plug porosity and permeability grouped according to sedimentary units. The trendlines correspond to the best fit, power-law distribution for each dataset and for the whole population (black trendline, R^2 value of 0.72).

Similar deformation patterns were documented in the region by D'Angelo et al. (2019). These latter authors interpreted left-lateral N–S and right-lateral NW-SE strike-slip faults as reactivated deep-rooted structures related to a N–S- to NNE-SSW-oriented contractional phase. Main migration routes of rising hydrothermal fluids may be related to these buried strike-slip fault zones cross-cutting the basement (D'Angelo

Table 3
Equivalent Porous Media (EPM) permeability calculated for the different CCS speleogenetic units considering an elementary cubic cell of 1 m width.

Speleogenetic units	Sedimentary units	K_P (mD)	K_N (mD)
Doline entrance	C	0.019	0.003
Upper storey	C–B2	1.30	0.74
Middle storey (siliciclastic seal)	B3	34.22	3.09
Middle storey (heterolithic seal)	B2	10.93	0.96
Middle storey (high-K silicified dolostones)	B1	1176.38	36.67
Lower storey	A	737.60	11.55

et al., 2019; Bertotti et al., 2020). Similar fault orientations occur in the CCS (Fig. 11A and E).

5.1.3. Stage 4 – main hypogene karst formation and silica reprecipitation

During stage 4 (Fig. 15) the rising hydrothermal fluids driven by pressure gradients and/or fluid buoyancy shaped the main hypogene karst in the CCS. The timing of the proposed hypogene large-scale karst porosity formation is still unknown. The occurrence of other hydrothermal events in the São Francisco Craton with similar mineral paragenesis (Kyle and Misi, 1997; Misi et al., 2005, 2012) and hypogene caves (Klimchouk et al., 2016) suggest a possible late Cambrian age. However, multiple phases of burial and denudation after the Early Cretaceous Pangea break-up occurred in the São Francisco Craton. The cumulative overburden above the present-day surface in the Chapada Diamantina quartzites (west of the study area) was estimated around 2–3 km (Japsen et al., 2012). This evidence suggests a complex and long burial-exhumation history for the carbonates of the Salitre *Fm*, during which hydrothermal fluids could have been able to drive dissolution generating large-scale karst porosity in hypogene settings.

The variability in petrophysical properties among the sedimentary units in the CCS (Fig. 13) determined the formation of the different speleogenetic storeys (and their associated morphologies). The lower storey hosted channelized vertical permeability pathways that acted as feeders for vertical fluid flow. In this storey, permeability pathways are mainly expressed by through-going fracture zones with high hydraulic apertures and good connectivity, which provided high vertical permeability ($K_P=10^2$ mD, Table 3). On the contrary, the middle storey is characterized by a sub-horizontal network of galleries developed mainly in the silicified unit (B1). The contrasting mechanical behavior of stiff chert nodules in the silicified layers with respect to surrounding dolostones, heteroliths, and marls, concentrated stress and caused fracture localization (Alvarez et al., 1976; Antonellini et al., 2020), producing networks of high permeability clustered joints (Fig. 12). As a result of high fracture permeability and early dissolution of silica during stage 3, K_P in unit B1 is the highest observed in the whole CCS ($K_P=10^3$ mD, Table 3), with values 2 to 3 orders of magnitude higher than those from units B2, B3, and C, and around 10 times the values observed in unit A. Unit B1 acted, therefore, as an inception horizon, defined as a lithostratigraphically-controlled element that favored hydraulic conductivity and the onset of dissolution (Lowe and Gunn, 1997).

At the same time, the heterolithic and siliciclastic rocks of units B2 and B3, despite having high porosity (~10–20%), have a low EPM permeability ($K_P=10^1$ mD, $K_N=10^0$ mD; Fig. 13, Table 3). This evidence, combined with the morphological observations on conduit geometries and distribution, indicates that they acted as low permeability buffering units promoting sub-horizontal flow in the underlying layers (Klimchouk et al., 2016; Balsamo et al., 2020). Additionally, these units are mostly composed of heterogeneous siliciclastic grains (i.e., K-feldspar, muscovite, quartz, kaolinite, chlorite, clay minerals), which are less soluble. Karst formation eventually occurred in focused discharge areas

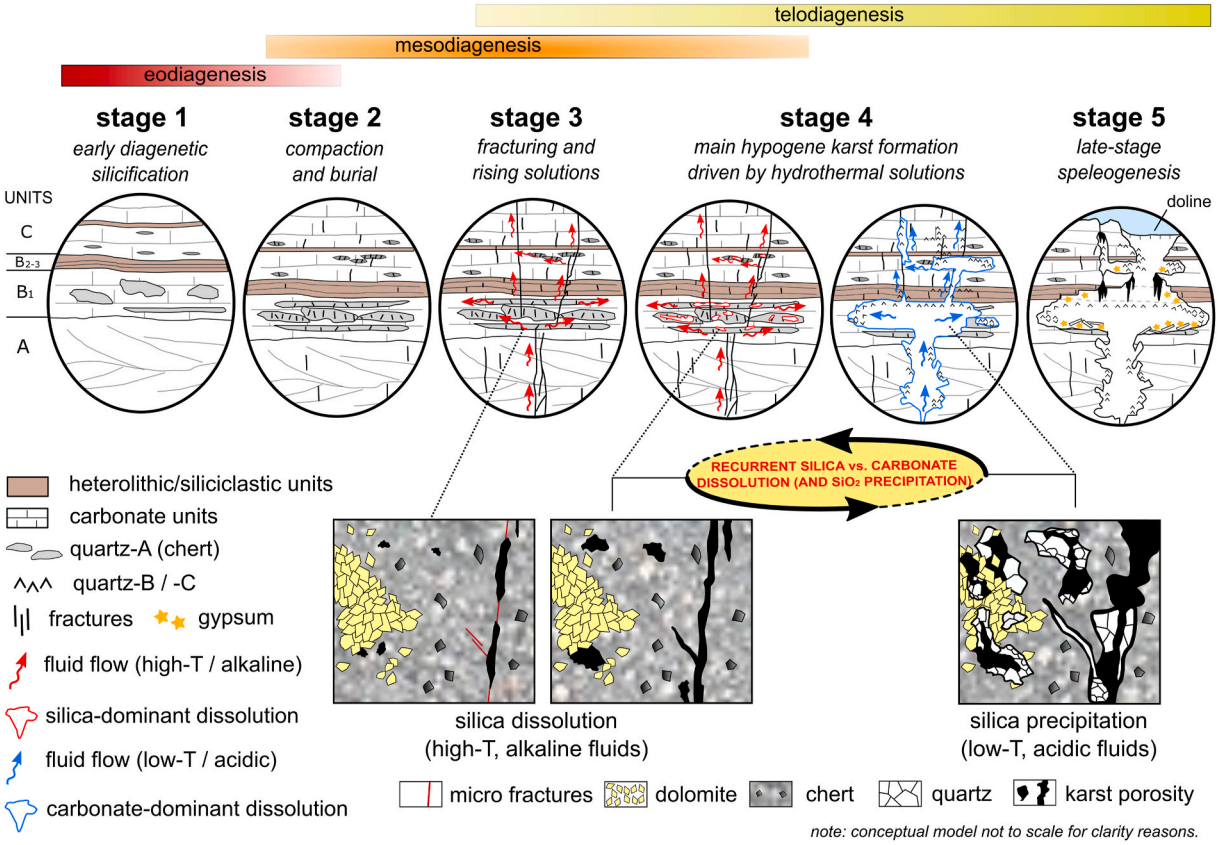

Fig. 15. Conceptual spatial-temporal development model for the Calixto Cave system at the micro-scale (vuggy karst porosity formation; lower part of the panel) and macro-scale (solutional human-sized cave passages; upper part of the panel). See the Discussion section 5.1 in the main text for further explanations.

along through-going FZ connecting the middle and upper storey (Figs. 13 and 15). Like unit B1, the occurrence of sub-horizontal solutional galleries in the upper storey is focused on the silicified ooidal grainstone and wackestone layers (Figs. 8 and 13) sealed at the top by intercalations of low permeability heterolith layers.

The very low porosity (~1–2%) and permeability of the dolomicrites in the upper sector of unit C (K_P=10^{-2} mD, K_N=10^{-3} mD; Table 3) is 5–6 orders of magnitude lower than the middle and lower storey permeability. This suggests that unit C acted as an efficient buffer for vertical fluid migration and karst formation, although a certain degree of discharge is expected to guarantee rising flow at the regional scale (Klimchouk et al., 2016).

The dissolution of carbonate and silicified layers to form the main conduit network required specific (and almost opposite) conditions, with the dolostone dissolution promoted by acidic and low temperature conditions, and the silica dissolution promoted by alkaline and high temperature conditions (Andreychouk et al., 2009; Cui et al., 2017). These two "end-members" of the hydrothermal fluids (at different temperature and/or geochemistry) do not necessarily imply distinct temporal intervals. On the contrary, we propose that a recurrent system of multiple silica-vs. carbonate-dominant dissolution (and silica reprecipitation) phases happened during stage 4 (Fig. 15). Hot and alkaline conditions promoted the silica-dominant dissolution of the silicified layers, enlarging and connecting the vuggy pores in chert nodules (mostly concentrated in unit B1). Water cooling and/or gradual pH changes in the hydrothermal flow system led towards more acidic conditions and caused the switch from silica-dominant dissolution to carbonate-dominant dissolution. Conduit morphology in the lower storey (spongework pattern, vertically extended rising conduits and rift-like feeders with reactive fronts) and widespread vuggy porosity in the dolostones indicate the weathering and corrosion effects of the hydrothermal fluids on these carbonate units. The precipitation of Qtz-B/Qtz-C and the associated hydrothermal mineral suite of Ca-sulfates, barite, muscovite, K-feldspar, Fe–Ti oxides, Fe–Cr spinels, sulfides, and phosphates (Table 1) occurred mainly in the lower sector of the cave below the heterolithic/siliciclastic units. The precipitation of these minerals caused partial occlusion of pore space in the vuggy and fracture porosity (Figs. 7, 9 and 15). Similar hydrothermal mineral assemblages are common also in the Brazilian pre-salt reservoirs (Lima and De Ros, 2019; Lima et al., 2020) and associated with MVT-type ore deposits found in the São Francisco Craton (Kyle and Misi, 1997; Cazarin et al., 2019, 2021).

5.1.4. Stage 5 – late-stage speleogenesis

The final stage of karst development (stage 5, Fig. 15) involved sulfuric acid formation in supergene conditions derived from pyrite oxidation within a shallow oxygenated (aerated) environment (Auler and Smart, 2003). This is indicated by the occurrence of iron oxide and hydroxide pseudomorphs replacing pyrite disseminated in the host rock, and secondary gypsum overgrowths and powders widely distributed in the cave system. The latter could be also the product of bat guano reactions. Condensation-corrosion processes likely enhanced the carbonate weathering in the cave system, as also suggested by the presence of condensation-corrosion features and dolostone weathering. Finally, collapse processes favored the widening of karst voids in the upper sector of the cave, ultimately causing the connection to the surface and the related transport of clastic sediments into the upper part of the CCS. All these late-stage processes overprinted the original dissolution morphologies of the karst system and amplified the dimensions of the passages observed today.

5.2. Cave spatial-morphological organization and implications for karst reservoirs

The 3D multistorey organization of the CCS is conceptually summarized in the sketch diagram of Fig. 16. The strong heterogeneity observed in the cave pattern and morphology is related to the lithological differences (Figs. 3A and 4) and the vertical distribution of fractures (Figs. 12 and 13). At the same time, petrophysical properties at the scale of the rock plugs indicate significant differences among the sedimentary units, especially those affected by silicification (Fig. 13). The variability in fracture spacing, individual fracture permeability, and petrophysical properties at the meso-scale (rock plugs) may be useful to recognize different hydrological units, fluid flow pathways and, therefore, speleogenetic storeys (Figs. 13 and 16; Table 3).

Estimated fracture permeability is calculated from present-day hydraulic apertures of the discontinuities but, at the time of speleogenesis, these apertures could have been significantly lower due to stress-dependency laws and fracture closing induced by loading (Holt, 1990; Min et al., 2004). Such calculations are beyond the scope of this work. However, based on our geomorphological observations of the cave pattern, morphology, and former flow pathways, we propose that the spatial organization of the karst system is expression of the structural-stratigraphic variability in the sequence.

In layered carbonate sequences of low primary porosity, through-going fractures (faults and fracture zones) are crucial for cross-formational fluid flow as they may determine the vertical connectivity of different sedimentary units. At the same time, the interplay between low-permeability buffering units and high-permeability units ($K>10^3$ mD) provided by high-aperture and closed-spaced (clustered) stratabound fractures may control horizontal permeability development and the formation of stratigraphically controlled voids. The combination of sub-seismic, meter-thick intercalations of low- ($K<1$ mD) and high-permeability ($K>10^3$ mD) units enhanced sub-horizontal karst formation in the CCS middle storey generating more than 1 km of large-scale, human-sized galleries (Fig. 16). Additionally, through-going fracture zones form vertical permeability pathways that crosscut the seal/buffer units, allowing fluids to rise into the upper sectors of the sequence, and promoting the formation of multiple levels of sub-horizontal cave passages at different stratigraphic positions (Fig. 16). The occurrence of similar multistorey karst patterns is not uncommon, especially in the Salitre *Fm* (Klimchouk, 2007; Klimchouk et al., 2016; Cazarin et al., 2019).

Our results provide new insights for the understanding of deep-seated karst formation and dissolution/precipitation involving silicified carbonate units. The spatial and morphological organization of dissolution features documented in the CCS (both at macroscopic and microscopic scale; Figs. 15 and 16) may be used as a conceptual analog or a proxy for many carbonate reservoirs where silicification and karst development are associated with specific sedimentary packages, like in the offshore pre-salt reservoirs of Brazil and Africa (Poros et al., 2017; Lima et al., 2020) or in the silicified reservoirs of the Tarim Basin (You et al., 2018). Karst cavities more than 2 m in diameter were observed at depths of 0.5–1.5 km in the Devonian and Carboniferous carbonate rocks of the Kizelovski basin and in the North Ural oil and gas basins (Andreychouk et al., 2009). Abundant cavities and macro-scale karst zones were intercepted by drillings at a depth down to 3–6 km in limestones, dolostones, and silicified carbonates of many basins worldwide (Zhao et al., 2018). Small-scale voids (vugs and fractures enlarged by dissolution) were also detected at depths larger than 5–10 km (Maximov et al., 1984; Andreychouk et al., 2009).

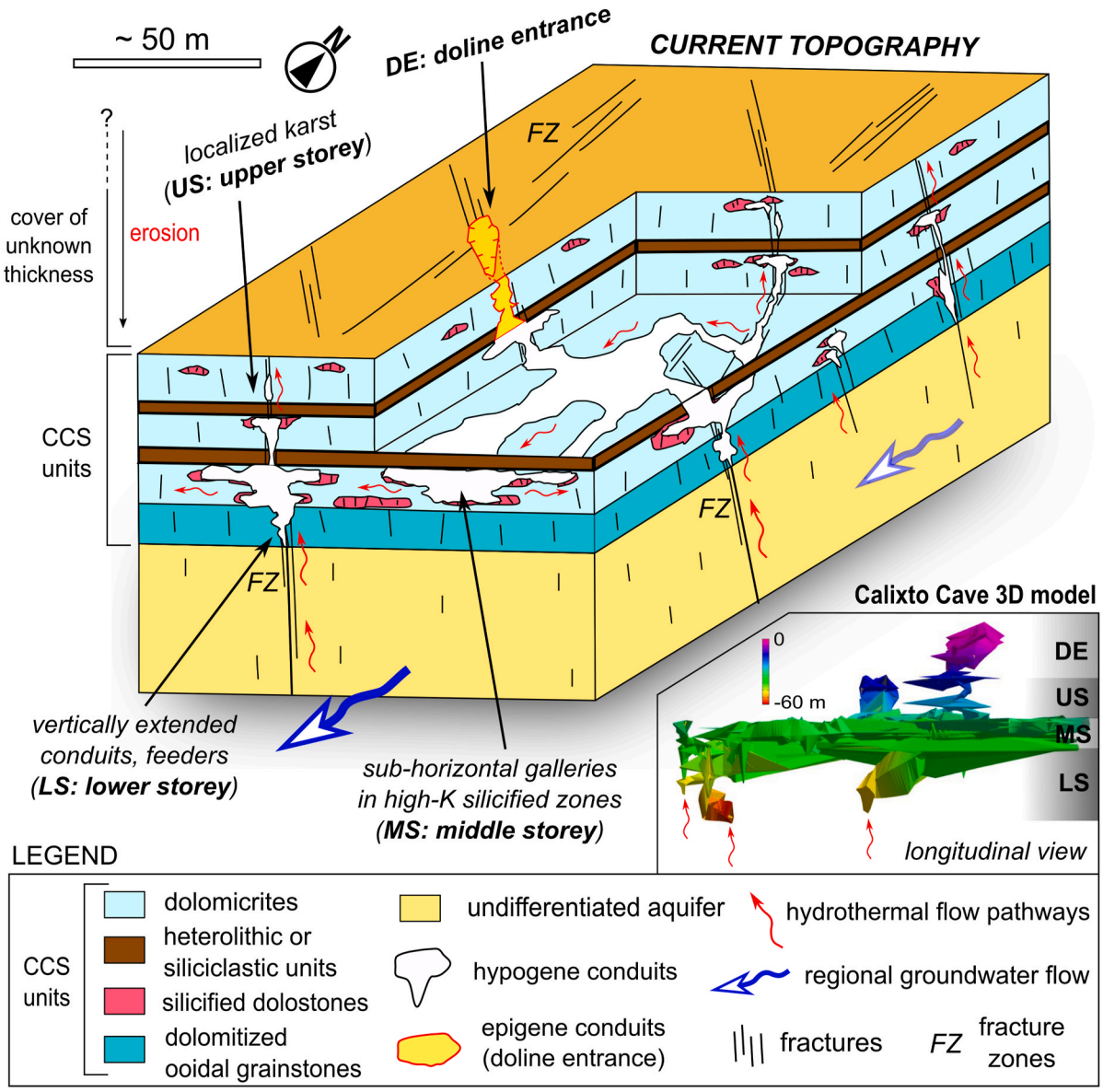

Fig. 16. Schematic block diagram illustrating the spatial-morphological organization of the CCS and the main fluid flow pathways. In the lower right corner, the 3D model of the cave (see also Fig. 3) is shown in a longitudinal section to visualize the vertical pattern of the multistorey system. Labels abbreviations: LS (lower storey), MS (middle storey), US (upper storey), DE (doline entrance).

The observations presented in this paper may help to better understand the relations between silicification and hypogene dissolution in deep-seated settings, contributing to the prediction of karst patterns at different scales. Furthermore, the CCS provided an enlightening example of the complex speleogenetic history that could affect ancient basins, where deep-seated dissolution (and precipitation) may drastically modify porosity in quartz-rich rocks such as highly silicified carbonates, commonly considered less prone to karst formation.

6. Conclusions

Our analytical and field studies support a conceptual model on the relation among stratigraphy, silicification, fracture patterns, petrophysical properties, and hypogene karst formation in the CCS. The main outcomes are summarized in the following points:

1) The mineralogy of the deposits and the geomorphological features of the cave suggest a deep-seated hypogene (hydrothermal) origin for the early karst phase. Early diagenetic silicification caused the replacement of dolomite grains and cement with microcrystalline quartz (up to 80-85 wt% of the bulk rock content). Below low permeability units, extensive mineral deposits are associated with blocky mega-quartz, chalcedony and a paragenesis of solid inclusions supporting the hydrothermal hypothesis.
2) The structural and stratigraphic variability in the CCS determined a strong anisotropy in fracture patterns, petrophysical properties, and fluid flow pathways. Fracturing concentrated in chert nodules causes a high intensity of open-mode fractures contributing to high permeability and dissolution localization. At the same time, through-going fracture zones and faults in the lower sector of the cave (characterized by low primary porosity and permeability) focused rising fluid flow along vertical permeability pathways (feeders and rising conduits).
3) Sedimentary units composed of heteroliths, marly dolostones, and fine-grained siliciclastic rocks represent a low-permeability seal/buffer unit that stopped/buffered vertical fluid flow. Through-going fracture zones breached these units, allowing vertical discharge and providing interconnectivity among the different sedimentary units.

4) The structural and stratigraphic variability in the CCS determined the formation of a complex 3D multistorey karst system. Silica-dominant dissolution (likely at T≥100–150 °C and pH≥8-9) promoted the formation of a stratigraphically-controlled inception horizon in the silicified and high-permeability dolostones of the middle storey. Multiple silica-vs. carbonate-dominant dissolution phases driven by hydrothermal solutions produced large-scale karst porosity, as well as the precipitation of the quartz-rich mineral deposits filling pore space and fractures. During telodiagenesis, collapses, condensation-corrosion, and karstification in supergene and epigene settings further amplified the conduit dimensions until today.
5) The results presented in this study contribute to expand our understanding of hypogene karst development in layered carbonate-siliciclastic units affected by silicification. The CCS example may be used to improve the conceptualization of predictive models on the spatial and morphological organization of buried hypogene conduit networks.

Credit authors statement

Luca Pisani: Conceptualization, Methodology, Software, Formal Analysis, Investigation, Validation, Data Curation, Writing – Original draft, Writing – Review & Editing, Visualization; **Marco Antonellini**: Conceptualization, Methodology, Formal Analysis, Investigation, Validation, Writing – Review & Editing, Supervision; **Francisco Hilario R. Bezerra**: Conceptualization, Investigation, Validation, Resources, Writing – Review & Editing, Supervision, Project Administration; **Cristina Carbone:** Methodology, Formal Analysis, Investigation, Writing – Review & Editing; **Augusto S. Auler:** Conceptualization, Investigation, Validation, Writing – Review & Editing; **Philippe Audra:** Investigation, Validation, Writing – Review & Editing; **Vincenzo La Bruna:** Investigation, Validation, Writing – Review & Editing; **Giovanni Bertotti:** Investigation, Validation, Writing – Review & Editing; **Fabrizio Balsamo:** Investigation, Validation, Writing – Review & Editing; **Cayo C.C. Pontes:** Investigation, Validation, Data Curation, Writing – Review & Editing; **Jo De Waele:** Conceptualization, Investigation, Validation, Resources, Writing – Review & Editing, Supervision.

Declaration of competing interest

The authors declare that they have no known competing financial interests or personal relationships that could have appeared to influence the work reported in this paper.

Acknowledgments

This research was carried out in association with the ongoing R&D project registered as ANP 20502-1, "*Processos e Propriedades em Reservatórios Carbonáticos Fraturados e Carstificados – POROCARSTE 3D" (UFRN/UNB/UFRJ/UFC/Shell Brasil/ANP*) – Porokarst – Processes and Properties in Fractured and Karstified Carbonate Reservoirs, sponsored by Shell Brasil under the ANP R&D levy as "*Compromisso de Investimento com Pesquisa e Desenvolvimento*". Cave map data were kindly provided by *Grupo Pierre Marin de Espeleologia* (GPME). Cave sampling was performed through SISBIO permit 63178/1. Many thanks to Alisson Jordão, Uilson Teixeira and Vicente Antonio Do Nascimento for the help during fieldwork.

We sincerely thank the Iramaia municipality (State of Bahia) and the Brazilian Federal Environmental Agency, *Instituto Chico Mendes*, for providing the access to the cave and the special permission for collecting rock samples. We also thank Giulio Viola and Paolo Garofalo for the access to the optical microscopy laboratory (University of Bologna), Fabio Gamberini for thin sections preparation, Giorgio Gasparotto for the access to the SEM laboratory in Bologna, and Gabriella Koltai, Yuri Dublyansky, and Christoph Spötl for the fruitful discussions. Finally, we thank Alexander Klimchouk and three anonymous reviewers for the detailed and constructive review that significantly improved our work.

Appendix A. Supplementary data

Supplementary data to this article can be found online at https://doi.org/10.1016/j.marpetgeo.2022.105611.

References

Almeida, F.F.M., Brito Neves, B.B., Dal Rè Carneiro, C., 2000. The origin and evolution of the South American Platform. Earth Sci. Rev. 50, 77–111. https://doi.org/10.1016/S0012-8252(99)00072-0.

Alvarez, W., Engelder, T., Lowrie, W., 1976. Formation of spaced cleavage and folds in brittle limestone by dissolution. Geology 4, 698–701.

Andreychouk, V., Dublyansky, Y., Ezhov, Y., Lisenin, G., 2009. Karst in the Earth's Crust: its Distribution and Principal Types. University of Silezia — Ukrainian Institute of Speleology and Karstology, Sosnovec–Simferopol, p. 72.

Antonellini, M., Cilona, A., Tondi, E., Zambrano, M., Agosta, F., 2014. Fluid flow numerical experiments of faulted porous carbonates, Northwest Sicily (Italy). Mar. Petrol. Geol. 55, 186–201. https://doi.org/10.1016/j.marpetgeo.2013.12.003.

Antonellini, M., Del Sole, L., Mollema, P.N., 2020. Chert nodules in pelagic limestones as paleo-stress indicators: a 3D geomechanical analysis. J. Struct. Geol. 132, 103979. https://doi.org/10.1016/j.jsg.2020.103979.

Araújo, R.E.B., La Bruna, V., Rustichelli, A., Bezerra, F.H.R., Xavier, M.M., Audra, P., Barbosa, J.A., Antonino, A.C.D., 2021. Structural and sedimentary discontinuities control the generation of karst dissolution cavities in a carbonate sequence, Potiguar Basin, Brazil. Mar. Petrol. Geol. 123, 104753. https://doi.org/10.1016/j.marpetgeo.2020.104753.

Audra, P., Palmer, A.N., 2015. Research frontiers in speleogenesis. Dominant processes, hydrogeological conditions and resulting cave patterns. Acta Carsol. 44 (3), 315–348. https://doi.org/10.3986/ac.v44i3.1960.

Audra, P., Mocochain, L., Bigot, J.-Y., Nobecourt, J.-C., 2009. Morphological indicators of speleogenesis: hypogenic speleogens. In: Klimchouk, A.B., Ford, D.C. (Eds.), Hypogenic Speleogenesis and Karst Hydrogeology of Artesian Basins: Simferopol, Ukraine. Ukrainian Institute of Speleology and Karstology, pp. 13–17.

Auler, A.S., 2017. Hypogene caves and karst of South America. In: Klimchouk, A., Palmer, A.N., De Waele, J., Auler, A.S., Audra, P. (Eds.), Hypogene Karst Regions and Caves of the World, Cave and Karst Systems of the World, vol. 2017. Springer International Publishing, Cham. https://doi.org/10.1007/978-3-319-53348-3.

Auler, A.S., Smart, P.L., 2003. The influence of bedrock-derived acidity in the development of surface and underground karst: evidence from the Precambrian carbonates of semi-arid northeastern Brazil. Earth Surf. Process. Landforms 28, 157–168. https://doi.org/10.1002/esp.443.

Balsamo, F., Bezerra, F.H.R., Klimchouk, A.B., Cazarin, C.L., Auler, A.S., Nogueira, F.C., Pontes, C., 2020. Influence of fracture stratigraphy on hypogene cave development and fluid flow anisotropy in layered carbonates, NE Brazil. Mar. Petrol. Geol. 114, 104207. https://doi.org/10.1016/j.marpetgeo.2019.104207.

Barton, N., Choubey, V., 1977. The shear strength of rock joints in theory and practice. Rock Mech. Rock Eng. 10 (1), 1–54.

Bertotti, G., Audra, P., Auler, A., Bezerra, F.H., de Hoop, S., Pontes, C., Prabhakaran, R., Lima, R., 2020. The Morro Vermelho hypogenic karst system (Brazil): stratigraphy, fractures, and flow in a carbonate strike-slip fault zone with implications for carbonate reservoirs. AAPG Bull. 104, 2029–2050. https://doi.org/10.1306/05212019150.

Bisdom, K., Bertotti, G., Nick, H.M., 2016. The impact of in-situ stress and outcrop-based fracture geometry on hydraulic aperture and upscaled permeability in fractured reservoirs. Tectonophysics 690, 63–75. https://doi.org/10.1016/j.tecto.2016.04.006.

Brito Neves, B.B., Fuck, R.A., Martins, M., 2014. The Brasiliano collage in South America: a review. Braz. J. Genet. 44, 493–518.

Burley, S.D., Kantorowicz, J.D., 1986. Thin section and SEM textural criteria for the recognition of cement-dissolution porosity in sandstones. Sedimentology 33 (4), 587–604.

Cacas, M.C., Ledoux, E., de Marsily, G., Tillie, B., Barbreau, A., Durand, E., Feuga, B., Peaudecerf, P., 1990. Modeling fracture flow with a stochastic discrete fracture network: calibration and validation: 1. The flow model. Water Resour. Res. 26 (3), 479–489. https://doi.org/10.1029/WR026i003p00479.

Caracciolo, L., Arribas, J., Ingersoll, R.V., Critelli, S., 2014. The diagenetic destruction of porosity in plutoniclastic petrofacies: the Miocene Diligencia and Eocene Maniobra formations, Orocopia Mountains, southern California, USA. In: Scott, R., Morton, A. (Eds.), Provenance Analyses in Hydrocarbon Exploration, vol. 386. Geol. Soc. London Sp. Pub, pp. 49–62. https://doi.org/10.1144/SP386.9 (1).

Cazarin, C.L., Bezerra, F.H.R., Borghi, L., Santos, R.V., Favoreto, J., Brod, J.A., Auler, A. S., Srivastava, N.K., 2019. The conduit-seal system of hypogene karst in Neoproterozoic carbonates in northeastern Brazil. Mar. Petrol. Geol. 101, 90–107. https://doi.org/10.1016/j.marpetgeo.2018.11.046.

Cazarin, C.L., van der Velde, R., Santos, R.V., Reijmer, J.J.G., Bezerra, F.H.R., Bertotti, G., La Bruna, V., Silva, D.C.C., de Castro, D.L., Srivastava, N.K., Barbosa, P. F., 2021. Hydrothermal activity along a strike-slip fault zone and host units in the São Francisco Craton, Brazil – implications for fluid flow in sedimentary basins. Precambrian Res. 106365 https://doi.org/10.1016/J.PRECAMRES.2021.106365.

Choquette, P.W., Pray, L.C., 1970. Geologic nomenclature and classification of porosity in sedimentary carbonates. AAPG Bull. 54, 207–244.
Columbu, A., Audra, P., Gázquez, F., D'Angeli, I.M., Bigot, J.Y., Koltai, G., Chiesa, R., Yu, T.L., Hu, H.M., Shen, C.C., Carbone, C., Heresanu, V., Nobécourt, J.C., De Waele, J., 2021. Hypogenic speleogenesis, late stage epigenic overprinting and condensation-corrosion in a complex cave system in relation to landscape evolution (Toirano, Liguria, Italy). Geomorphology 376, 107561. https://doi.org/10.1016/j.geomorph.2020.107561.
Condie, K.C., 2002. The supercontinent cycle: are there two patterns of cyclicity? J. Afr. Earth Sci. 35, 179–183. https://doi.org/10.1016/S0899-5362(02)00005-2.
Cui, H., Kaufman, A.J., Xiao, S., Zhou, C., Liu, X.M., 2017. Was the Ediacaran Shuram Excursion a globally synchronized early diagenetic event? Insights from methane-derived authigenic carbonates in the uppermost Doushantuo Formation, South China. Chem. Geol. 450, 59–80. https://doi.org/10.1016/j.chemgeo.2016.12.010.
D'Angelo, T., Barbosa, M.S.C., Danderfer Filho, A., 2019. Basement controls on cover deformation in eastern Chapada Diamantina, northern São Francisco Craton, Brazil: insights from potential field data. Tectonophysics 772, 228231. https://doi.org/10.1016/j.tecto.2019.228231.
De Luca, P.H.V., Matias, H., Carballo, J., Sineva, D., Pimentel, G.A., Tritlla, J., Esteban, M., Loma, R., Alonso, J.L.A., Jiménez, R.P., Pontet, M., Martinez, P.B., Vega, V., 2017. Breaking barriers and paradigms in presalt exploration: the Pão de Açúcar discovery (Offshore Brazil). AAPG Memoir 113, 177–193. https://doi.org/10.1306/13572007M1133686.
De Waele, J., Plan, L., Audra, P., 2009. Recent developments in surface and subsurface karst geomorphology: an introduction. Geomorphology 106, 1–8. https://doi.org/10.1016/j.geomorph.2008.09.023.
De Waele, J., Audra, P., Madonia, G., Vattano, M., Plan, L., D'Angeli, I.M., Bigot, J.Y., Nobécourt, J.C., 2016. Sulfuric acid speleogenesis (SAS) close to the water table: examples from southern France, Austria, and Sicily. Geomorphology 253, 452–467. https://doi.org/10.1016/j.geomorph.2015.10.019.
Del Sole, L., Antonellini, M., Soliva, R., Ballas, G., Balsamo, F., Viola, G., 2020. Structural control on fluid flow and shallow diagenesis: insights from calcite cementation along deformation bands in porous sandstones. Solid Earth 11, 2169–2195. https://doi.org/10.5194/se-11-2169-2020.
Dong, S., You, D., Guo, Z., Guo, C., Chen, D., 2018. Intense silicification of Ordovician carbonates in the Tarim Basin: constraints from fluid inclusion Rb–Sr isotope dating and geochemistry of quartz. Terra. Nova 30, 406–413. https://doi.org/10.1111/ter.12356.
Dove, P.M., 1999. The dissolution kinetics of quartz in aqueous mixed cation solutions. Geochem. Cosmochim. Acta 63 (22), 3715–3727. https://doi.org/10.1016/S0016-7037(99)00218-5.
Dove, P.M., Nix, C.J., 1997. The influence of the alkaline earth cations, magnesium, calcium, and barium on the dissolution kinetics of quartz. Geochem. Cosmochim. Acta 61 (16), 3329–3340. https://doi.org/10.1016/S0016-7037(97)00217-2.
Dunham, R.J., 1962. Classification of carbonate rocks according to depositional texture. In: Ham, W.E. (Ed.), Classification of Carbonates Rocks. AAPG Memoir I, pp. 108–121.
Embry, A.F., Klovan, J.E., 1971. A late Devonian reef tract on northeastern Banks Island. NWT. Bull. Can. Petrol. Geol. 19, 730–781.
Ennes-Silva, R.A., Bezerra, F.H.R., Nogueira, F.C.C., Balsamo, F., Klimchouk, A., Cazarin, C.L., Auler, A.S., 2016. Superposed folding and associated fracturing influence hypogene karst development in Neoproterozoic carbonates, São Francisco Craton, Brazil. Tectonophysics 666, 244–259. https://doi.org/10.1016/j.tecto.2015.11.006.
Flodin A., Eric, Durlofski J., Louis, Aydin, Atilla, 2004. Upscaled models of flow and transport in faulted sandstone: boundary condition effects and explicit fracture modelling. Petrol. Geosci. 10 (2), 173–181. https://doi.org/10.1144/1354-079303-587.
Ford, D.C., Williams, P.W., 2007. Karst Hydrogeology and Geomorphology. John Wiley & Sons, p. 562.
Girard, J.-P., San Miguel, G., 2017. Evidence of high temperature hydrothermal regimes in the pre-salt series, Kwanza Basin, offshore Angola. In: American Association of Petroleum Geologists Annual Convention and Exhibition. Houston, Texas, USA, Abstracts).
Giuffrida, A., La Bruna, V., Castelluccio, P., Panza, E., Rustichelli, A., Tondi, E., Giorgioni, M., Agosta, F., 2019. Fracture simulation parameters of fractured reservoirs: analogy with outcropping carbonates of the Inner Apulian Platform. southern Italy. J. Struct. Geol. 123, 18–41.
Giuffrida, A., Agosta, F., Rustichelli, A., Panza, E., La Bruna, V., Eriksson, M., Torrieri, S., Giorgioni, M., 2020. Fracture stratigraphy and DFN modelling of tight carbonates, the case study of the Lower Cretaceous carbonates exposed at the Monte Alpi (Basilicata, Italy). Mar. Petrol. Geol. 112, 104045. https://doi.org/10.1016/j.marpetgeo.2019.104045.
Goldscheider, N., Mádl-Szőnyi, J., Erőss, A., Schill, E., 2010. Thermal water resources in carbonate rock aquifers. Hydrogeol. J. 18, 1303–1318.
Guha Roy, D., Singh, T.N., 2016. Fluid flow through rough rock fractures: parametric study. Int. J. GeoMech. 16 (3), 04015067 https://doi.org/10.1061/(ASCE)GM.1943-5622.0000522.
Guimarães, J.T., Misi, A., Pedreira, A.J., Dominguez, J.M.L., 2011. The Bebedouro formation, Una group, Bahia (Brazil). Geol. Soc. Mem. 36, 503–508. https://doi.org/10.1144/M36.47.
Gunnarsson, I., Arnórsson, S., 2000. Amorphous silica solubility and the thermodynamic properties of H_4SiO_4 in the range of 0° to 350°C at P(sat). Geochem. Cosmochim. Acta 64, 2295–2307. https://doi.org/10.1016/S0016-7037(99)00426-3.
Heeb, B., 2009. An all-in-one electronic cave surveying device. CREG J 72, 8–10.
Hesse, R., 1989. Silica diagenesis: origin of inorganic and replacement cherts. Earth Sci. Rev. 26, 253–284. https://doi.org/10.1016/0012-8252(89)90024-X.
Higgs, R., 1979. Quartz-grain surface features of Mesozoic-Cenozoic sands from the Labrador and western Greenland continental margins. J. Sediment. Res. 49, 599–610.
Holt, R.M., 1990. Permeability reduction induced by a nonhydrostatic stress field. SPE Form. Eval. 5, 444–448. https://doi.org/10.2118/19595-PA.
Itamiya, H., Sugita, R., Sugai, T., 2019. Analysis of the surface microtextures and morphologies of beach quartz grains in Japan and implications for provenance research. Prog. Earth Planet. Sci. 6, 1–14. https://doi.org/10.1186/s40645-019-0287-9.
Japsen, P., Bonow, J.M., Green, P.F., Cobbold, P.R., Chiossi, D., Lilletveit, R., Magnavita, L.P., Pedreira, A.J., 2012. Episodic burial and exhumation history of NE Brazil after opening of the south Atlantic. GSA Bull. 124, 800–816. https://doi.org/10.1130/B30515.1.
Klimchouk, A., 2007. Hypogene Speleogenesis: Hydrogeological and Morphometric Perspective. National Cave and Karst Research Institute, Carlsbad, p. 106.
Klimchouk, A., 2009. Morphogenesis of hypogenic caves. Geomorphology 106, 100–117. https://doi.org/10.1016/j.geomorph.2008.09.013.
Klimchouk, A., 2019. Speleogenesis, hypogenic. In: White, W.B., Culver, D.C., Pipan, T. (Eds.), Encyclopedia of Caves, third ed. Academic Press, New York, pp. 974–988.
Klimchouk, A., Ford, D.C., Palmer, A.N., Dreybrodt, W., 2000. Speleogenesis: Evolution of Karst Aquifers. National Speleological Society, Huntsville, Al.
Klimchouk, A.B., Andreychouk, V.N., Turchinov, I.I., 2009. The Structural Prerequisites of Speleogenesis in Gypsum in the Western Ukraine, second ed. University of Silesia - Ukrainian Institute of Speleology and Karstology, Sosnowiec-Simferopol, p. 96.
Klimchouk, A., Auler, A.S., Bezerra, F.H.R., Cazarin, C.L., Balsamo, F., Dublyansky, Y., 2016. Hypogenic origin, geologic controls, and functional organization of a giant cave system in Precambrian carbonates, Brazil. Geomorphology 253, 385–405 ttps://doi.org/10.1016/j.geomorph.2015.11.002.
Klinkenberg, L.J., 1941. The permeability of porous media to liquids and gases. In: Drilling and Production Practice. American Petroleum Institute, pp. 200–213.
Kornilov, V.F., 1978. The temperature regime of formation of the mercury–antimony mineralization (Southern Kirghizia). In: Ermakov, N.P. (Ed.), Thermobarogeochemistry of the Earth's Crust. Nauka, Moscow, pp. 155–161.
Kyle, J.R., Misi, A., 1997. Origin of Zn-Pb-Ag sulfide mineralization within upper proterozoic phosphate-rich carbonate strata, Irêce Basin, Bahia, Brazil. Int. Geol. Rev. 39, 383–399.
La Bruna, V., Bezerra, F.H.R., Souza, V.H.P., Maia, R.P., Auler, A.S., Araújo, R.E.B., Cazarin, C.L., Rodrigues, M.A.F., Vieira, L.C., Sousa, M.O.L., 2021. High-permeability zones in folded and faulted silicified carbonate rocks – implications for karstified carbonate reservoirs. Mar. Petrol. Geol. 128, 105046. https://doi.org/10.1016/j.marpetgeo.2021.105046.
Lavrov, A., 2017. Fracture permeability under normal stress: a fully computational approach. J. Pet. Explor. Prod. Technol. 7, 181–194. https://doi.org/10.1007/s13202-016-0254-6.
Lei, Q., Latham, J.P., Tsang, C.F., 2017. The use of discrete fracture networks for modelling coupled geomechanical and hydrological behaviour of fractured rocks. Comput. Geotech. 85, 151–176. https://doi.org/10.1016/j.compgeo.2016.12.024.
Leven, J.A., 1961. Problems of origin of optical-quality fluorite from deposits of the Zeravshan–Gissar Mountains. Trans. Samarkand Univ. 16, 35–51.
Lima, B.E.M., De Ros, L.F., 2019. Deposition, diagenetic and hydrothermal processes in the Aptian Pre-Salt lacustrine carbonate reservoirs of the northern Campos Basin, offshore Brazil. Sediment. Geol. 383, 55–81. https://doi.org/10.1016/j.sedgeo.2019.01.006.
Lima, B.E.M., Tedeschi, L.R., Pestilho, A.L.S., Santos, R.V., Vazquez, J.C., Guzzo, J.V.P., De Ros, L.F., 2020. Deep-burial hydrothermal alteration of the Pre-Salt carbonate reservoirs from northern Campos Basin, offshore Brazil: evidence from petrography, fluid inclusions, Sr, C and O isotopes. Mar. Petrol. Geol. 113, 104143. https://doi.org/10.1016/j.marpetgeo.2019.104143.
Lønøy, B., Tveranger, J., Pennos, C., Whitaker, F., Lauritzen, S.E., 2020. Geocellular rendering of cave surveys in paleokarst reservoir models. Mar. Petrol. Geol. 122, 104652. https://doi.org/10.1016/j.marpetgeo.2020.104652.
Lyu, X., Zhu, G., Liu, Z., 2020. Well-controlled dynamic hydrocarbon reserves calculation of fracture–cavity karst carbonate reservoirs based on production data analysis. J. Pet. Explor. Prod. Technol. 10, 2401–2410. https://doi.org/10.1007/s13202-020-00881-w.
Lovering, T.S., Tweto, O., Loweing, T.G., 1978. Ore Deposits of the Gilman District, Eagle Country, Colorado. U.S. Geological Survey Professional, p. 90. Paper 1017.
Lowe, D.J., Gunn, J., 1997. Carbonate speleogenesis: an inception horizon hypothesis. Acta Carsol. 26 (2), 457–488.
Maliva, R.G., Siever, R., 1989. Nodular chert formation in carbonate rocks. J. Geol. 97, 421–433.
Marin-Carbonne, J., Robert, F., Chaussidon, M., 2014. The silicon and oxygen isotope compositions of Precambrian cherts: a record of oceanic paleo-temperatures? Precambrian Res. 247, 223–234. https://doi.org/10.1016/j.precamres.2014.03.016.
Marrett, R., Ortega, O., Kelsey, C., 1999. Extent Power-law Scaling Nat. Fractures Rock: Geology 27 (9), 799–802.
Maximov, S.P., Zolotov, A.N., Lodzhevskaya, M.I., 1984. Tectonic conditions for oil and gas generation and distribution on ancient platforms. J. Petrol. Geol. 7 (3), 329–340.
Mazzullo, S.J., 2004. Overview of porosity evolution in carbonate reservoirs. Kansas Geol. Soc. Bull. 79 (1, 2), 1–19.
Mazzullo, S.J., Rieke, H.H., Chilingarian, G., 1996. Carbonate reservoir characterization: a geological-engineering analysis, Part II. Dev. Petrol. Sci. 44, 994 (Elsevier).
Mecchia, M., Sauro, F., Piccini, L., Columbu, A., De Waele, J., 2019. A hybrid model to evaluate subsurface chemical weathering and fracture karstification in quartz

sandstone. J. Hydrol. 572, 745–760. https://doi.org/10.1016/j.jhydrol.2019.02.026.
Min, K.B., Rutqvist, J., Tsang, C.F., Jing, L., 2004. Stress-dependent permeability of fractured rock masses: a numerical study. Int. J. Rock Mech. Min. Sci. 41, 1191–1210. https://doi.org/10.1016/j.ijrmms.2004.05.005.
Ming, X.R., Liu, L., Yu, M., Bai, H.G., Yu, L., Peng, X.L., Yang, T.H., 2016. Bleached mudstone, iron concretions, and calcite veins: a natural analogue for the effects of reducing CO2-bearing fluids on migration and mineralization of iron, sealing properties, and composition of mudstone cap rocks. Geofluids 16, 1017–1042. https://doi.org/10.1111/GFL.12203.
Misi, A., 1993. A Sedimentação Carbonática do Proterozóico Superior no Cráton do São Francisco: Evolução Diagenética e Estratigrafia Isotópica. II Symposium on the São Francisco Craton. Extended abstracts. Salvador, Brazil, pp. 192–193.
Misi, A., Veizer, J., 1998. Neoproterozoic carbonate sequences of the Una Group, Irêce Basin, Brazil: chemostratigraphy, age and correlations. Precambrian Res. 89, 87–100. https://doi.org/10.1016/S0301-9268(97)00073-9.
Misi, A., Iyer, S.S.S., Coelho, C.E.S., Tassinari, C.C.G., Franca-Rocha, W.J.S., Cunha, I.D. A., Gomes, A.S.R., de Oliveira, T.F., Teixeira, J.B.G., Filho, V.M.C., 2005. Sediment hosted lead–zinc deposits of the Neoproterozoic Bambuí Group and correlative sequences, São Francisco craton, Brazil: a review and a possible metallogenic evolution model. Ore Geol. Rev. 26, 263–304.
Misi, A., Kaufman, A.J., Veizer, J., Powis, K., Azmy, K., Boggiani, P.C., Gaucher, C., Teixeira, J.B.G., Sanches, A.L., Iyer, S.S., 2007. Chemostratigraphic correlation of neoproterozoic successions in South America. Chem. Geol. 237, 22–45. https://doi.org/10.1016/j. chemgeo.2006.06.019.
Misi, A., Kaufman, A.J., Azmy, K., Dardenne, M.A., 2011. Neoproterozoic successions of the São Francisco craton, Brazil: the Bambuí, Una, Vazante and Vaza Barris/Miaba groups and their glaciogenic deposits. Geol. Rec. Neoproterozoic Glaciat. 36, 509–522. https://doi.org/10.1144/M36.48.
Misi, A., Batista, J., Teixeira, G., 2012. Mapa Metalogenético Digital do Estado da Bahia e Principais Províncias Minerais. Série Publicações Especiais 11.
Mitsiuk, B.N., 1974. Vzaimodeistvie Kremnezema S Vodoy V Hydrotermalnych Usloviach (Interaction between Silica and Water in Hydrothermal Conditions). Naukova Dumka, Kiev, p. 86 (In Russian).
Montanari, D., Minissale, A., Doveri, M., Gola, G., Trumpy, E., Santilano, A., Manzella, A., 2017. Geothermal resources within carbonate reservoirs in western Sicily (Italy): a review. Earth Sci. Rev. 169, 180–201. https://doi.org/10.1016/J.EARSCIREV.2017.04.016.
Morad, S., Ketzer, J.M., Ros, L.F. De, 2000. Spatial and temporal distribution of diagenetic alterations in siliciclastic rocks: implications for mass transfer in sedimentary basins. Sedimentology 47, 95–120. https://doi.org/10.1046/J.1365-3091.2000.00007.X.
Myers, R., Aydin, A., 2004. The evolution of faults formed by shearing across joint zones in sandstone. J. Struct. Geol. 26 (5), 947–966.
Myrow, P.M., Southard, J.B., 1996. Tempestite deposition. J. Sediment. Res. 66, 875–887.
Odling, N.E., Gillespie, P., Bourgine, B., Castaing, C., Chilés, J.P., Christensen, N.P., Fillion, E., Genter, A., Olsen, C., Thrane, L., Trice, R., Aarseth, E., Walsh, J.J., Watterson, J., 1999. Variations in fracture system geometry and their implications for fluid flow in fractured hydrocarbon reservoirs. Petrol. Geosci. 5, 373–384. https://doi.org/10.1144/petgeo.5.4.373.
Olsson, R., Barton, N., 2001. An improved model for hydromechanical coupling during shearing of rock joints. Int. J. Rock Mech. Min. Sci. 38, 317–329.
Ortega, O.J., Marrett, R.A., Laubach, S.E., 2006. A scale-independent approach to fracture intensity and average spacing measurement. AAPG Bull. 90, 193–208. https://doi.org/10.1306/08250505059.
Packard, J.J., Al-Aasm, I., Samson, I., 2001. A Devonian hydrothermal chert reservoir: the 225 bcf Parkland field, British Columbia, Canada. AAPG Bulletin 85 (1), 51–84.
Palmer, A.N., 2000. Hydrogeologic control of cave patterns. In: Klimchouk, A., Ford, D. C., Palmer, A.N., Dreybrodt, W. (Eds.), Speleogenesis: Evol. Karst Aquifers 240, 145–146. https://doi.org/10.1016/s0022-1694(00)00341-3, 2000.
Peucat, J.J., Figueiredo Barbosa, J.S., Conceição de Araújo Pinho, I., Paquette, J.L., Martin, H., Fanning, C.M., Beatriz de Menezes Leal, A., Cruz, S., 2011. Geochronology of granulites from the south Itabuna-Salvador-Curaçá Block, São Francisco Craton (Brazil): Nd isotopes and U-Pb zircon ages. J. South Am. Earth Sci. 31, 397–413. https://doi.org/10.1016/j.jsames.2011.03.009.
Philipp, S.L., Afşar, F., Gudmundsson, A., 2013. Effects of mechanical layering on hydrofracture emplacement and fluid transport in reservoirs. Front. Earth Sci. 1 https://doi.org/10.3389/feart.2013.00004. Article 4.
Pisani, L., Antonellini, M., De Waele, J., 2019. Structural control on epigenic gypsum caves: evidences from Messinian evaporites (Northern Apennines, Italy). Geomorphology 332, 170–186. https://doi.org/10.1016/j.geomorph.2019.02.016.
Pisani, L., Antonellini, M., D'Angeli, I.M., De Waele, J., 2021. Structurally controlled development of a sulfuric hypogene karst system in a fold-and-thrust belt (Majella Massif, Italy). J. Struct. Geol. 145, 104305. https://doi.org/10.1016/j.jsg.2021.104305.
Pontes, C.C.C., Bezerra, F.H.R., Bertotti, G., La Bruna, V., Audra, P., De Waele, J., Auler, A.S., Balsamo, F., De Hoop, S., Pisani, L., 2021. Flow pathways in multiple-direction fold hinges: implications for fractured and karstified carbonate reservoirs. J. Struct. Geol. 146, 104324. https://doi.org/10.1016/j.jsg.2021.104324.
Poros, Z., Jagniecki, E., Luczaj, J., Kenter, J., Gal, B., Correa, T.S., Ferreira, E., McFadden, K.A., Elifritz, A., Heumann, M., Johnston, M., Matt, V., 2017. Origin of silica in pre-salt carbonates, Kwanza Basin, Angola. In: American Association of Petroleum Geologists Annual Convention and Exhibition. Houston, Texas, USA).
Rimstidt, J.D., 1997. Quartz solubility at low temperatures. Geochem. Cosmochim. Acta 61, 2553–2558.
Reineck, H., Wunderlich, F., 1968. Classification and origin of flaser and lenticular bedding. Sedimentology 11, 99–104.
Rolland, A., Toussaint, R., Baud, P., Conil, N., Landrein, P., 2014. Morphological analysis of stylolites for paleostress estimation in limestones. Int. J. Rock Mech. Min. Sci. 67, 212–225. https://doi.org/10.1016/J.IJRMMS.2013.08.021.
Salvini, F., 2004. Daisy 3: the Structural Data Integrated System Analyzer Software. University of Roma Tre, Rome available at: http://host.uniroma3.it/progetti/fralab/Downloads/Programs/.
Santana, A., Chemale, F., Scherer, C., Guadagnin, F., Pereira, C., Santos, J.O.S., 2021. Paleogeographic constraints on source area and depositional systems in the neoproterozoic Irecê basin, São Francisco craton. J. South Am. Earth Sci. 109, 103330. https://doi.org/10.1016/j.jsames.2021.103330.
Sauro, F., De Waele, J., Onac, B.P., Galli, E., Dublyansky, Y., Baldoni, E., Sanna, L., 2014. Hypogenic speleogenesis in quartzite: the case of Corona 'e Sa Craba Cave (SW Sardinia, Italy). Geomorphology 211, 77–88. https://doi.org/10.1016/j.geomorph.2013.12.031.
Shanmugan, G., Higgins, J.B., 1988. Porosity enhancement from chert dissolution beneath neocomian unconformity: Ivishak formation, North slope, Alaska. AAPG Bull. 72 (5), 523–535.
Siever, R., 1962. Silica solubility, 0°C - 200°C, and the diagenesis of siliceous sediments. J. Geol. 70, 127–150.
Smeraglia, L., Giuffrida, A., Grimaldi, S., Pullen, A., La Bruna, V., Billi, A., Agosta, F., 2021. Fault-controlled upwelling of low-T hydrothermal fluids tracked by travertines in a fold-and-thrust belt, Monte Alpi, southern Apennines, Italy. J. Struct. Geol. 144, 104276. https://doi.org/10.1016/j.jsg.2020.104276.
Souza, V.H.P., Bezerra, F.H.R., Vieira, L.C., Cazarin, C.L., Brod, J.A., 2021. Hydrothermal silicification confined to stratigraphic layers: implications for carbonate reservoirs. Mar. Petrol. Geol. 124, 104818. https://doi.org/10.1016/j.marpetgeo.2020.104818.
Spötl, C., Dublyansky, Y., Koltai, G., Cheng, H., 2021. Hypogene speleogenesis and paragenesis in the Dolomites. Geomorphology 382, 107667. https://doi.org/10.1016/J.GEOMORPH.2021.107667.
Teixeira, J.B.G., Misi, A., Silva, M.G., 2007. Supercontinent evolution and the proterozoic metallogeny of south America. Gondwana Res. 11, 346–361. https://doi.org/10.1016/j.gr.2006.05.009.
Terzaghi, R.D., 1965. Source of error in joint surveys. Geotechnique 15 (3), 287–304.
Tsykin, R.A., 1989. Paleokarst of the union of Soviet Socialistic Republics. In: Bosák, P., Ford, D.C., Głazek, J., Horáček, I. (Eds.), Paleokarst: A Systematic and Regional Review. Vidala Academia, Praha, pp. 253–295.
Van Golf-Racht, T., 1982. Fundamentals of Fractured Reservoir Engineering. Elsevier, Amsterdam, p. 732.
Wray, R.A., Sauro, F., 2017. An updated global review of solutional weathering processes and forms in quartz sandstones and quartzites. Earth Sci. Rev. 171, 520–557. https://doi.org/10.1016/j.earscirev.2017.06.008.
Wu, M.B., Wang, Y., Zheng, M.L., Zhang, W.B., Liu, C.Y., 2007. The hydrothermal karstification and its effect on Ordovician carbonate reservoir in Tazhong uplift of Tarim Basin, Northwest China. Sci. China Earth Sci. 50 (2), 103–113. https://doi.org/10.1007/s11430-007-6026-x.
Xu, X., Chen, Q., Chu, C., Li, G., Liu, C., Shi, Z., 2017. Tectonic evolution and paleo-karstification of carbonate rocks in the Paleozoic Tarim Basin. Carb. & Evap. 32, 487–496.
You, D., Han, J., Hu, W., Qian, Y., Chen, Q., Xi, B., Ma, H., 2018. Characteristics and formation mechanisms of silicified carbonate reservoirs in well SN4 of the Tarim Basin. Energy Explor. Exploit. 36, 820–849. https://doi.org/10.1177/0144598718757515.
Zambrano, M., Tondi, E., Korneva, I., Panza, E., Agosta, F., Janiseck, J.M., Giorgioni, M., 2016. Fracture properties analysis and discrete fracture network modelling of faulted tight limestones, Murge Plateau. Italy. Ital. J. Geosci. 135, 55–67. https://doi.org/10.3301/IJG.2014.42.
Zhao, X., Jin, F., Zhou, L., Wang, Q., Pu, X., 2018. Re-exploration Programs for Petroleum-Rich Sags in Rift Basins. Gulf Professional Publishing, p. 642.
Zhang, J.J., 2019. Rock physical and mechanical properties. In: Applied Petroleum Geomechanics. Elsevier, pp. 29–83. https://doi.org/10.1016/b978-0-12-814814-3.00002-2.
Zheng, J., Wang, X., Lü, Q., Sun, H., Guo, J., 2020. A new determination method for the permeability tensor of fractured rock masses. J. Hydrol. 585, 124811.
Zhou, X., Chen, D., Qing, H., Qian, Y., Wang, D., 2014. Submarine silica-rich hydrothermal activity during the earliest Cambrian in the Tarim basin, northwest China. Int. Geol. Rev. 56, 1906–1918. https://doi.org/10.1080/00206814.2014.968885.